NeuroImage 133 (2016) 207–223

Contents lists available at ScienceDirect

NeuroImage

journal homepage: www.elsevier.com/locate/ynimg

Bingham–NODDI: Mapping anisotropic orientation dispersion of neurites using diffusion MRI

Maira Tariq [a,*], Torben Schneider [b], Daniel C. Alexander [a], Claudia A. Gandini Wheeler-Kingshott [b,c], Hui Zhang [a]

[a] Department of Computer Science & Centre for Medical Image Computing, University College London, UK
[b] NMR Research Unit, Department of Neuroinflammation, UCL Institute of Neurology, University College London, London, UK
[c] Brain Connectivity Center, C. Mondino National Neurological Institute, Pavia, Italy

ARTICLE INFO

Article history:
Received 27 July 2015
Accepted 20 January 2016
Available online 28 January 2016

Keywords:
Anisotropic orientation dispersion
NODDI
Diffusion MRI
Bingham distribution
Neurite morphology

ABSTRACT

This paper presents Bingham–NODDI, a clinically-feasible technique for estimating the anisotropic orientation dispersion of neurites. Direct quantification of neurite morphology on clinical scanners was recently realised by a diffusion MRI technique known as neurite orientation dispersion and density imaging (NODDI). However in its current form NODDI cannot estimate anisotropic orientation dispersion, which is widespread in the brain due to common fanning and bending of neurites. This work proposes Bingham–NODDI that extends the NODDI formalism to address this limitation. Bingham–NODDI characterises anisotropic orientation dispersion by utilising the Bingham distribution to model neurite orientation distribution. The new model estimates the extent of dispersion about the dominant orientation, separately along the primary and secondary dispersion orientations. These estimates are subsequently used to estimate the overall dispersion about the dominant orientation and the dispersion anisotropy. We systematically evaluate the ability of the new model to recover these key parameters of anisotropic orientation dispersion with standard NODDI protocol, both *in silico* and *in vivo*. The results demonstrate that the parameters of the proposed model can be estimated without additional acquisition requirements over the standard NODDI protocol. Thus anisotropic dispersion can be determined and has the potential to be used as a marker for normal brain development and ageing or in pathology. We additionally find that the original NODDI model is robust to the effects of anisotropic orientation dispersion, when the quantification of anisotropic dispersion is not of interest.

Introduction

Axons and dendrites, collectively known as neurites, are the projections from the cell body of a neuron; they are the structural underpinnings of brain functions. Neurite morphology, quantified using histological analysis of postmortem tissue, is the most accurate and reliable means for understanding the development (Conel, 1939), ageing (Jacobs et al., 1997), function (Jacobs et al., 2001) and pathology (Fiala et al., 2002) of the brain. Accessing such information *in vivo* in humans has been of great interest as it can enable a dynamic view of the brain function and development, in health and disease.

Diffusion magnetic resonance imaging (MRI) can non-invasively probe the microstructure and thus has become an indispensable tool for *in vivo* assessment of neurite morphology. Diffusion tensor imaging (DTI) (Basser et al., 1994), the standard diffusion MRI technique in neuroimaging, provides sensitivity to neurite morphology but cannot quantify neurite-specific measures such as their density and orientation dispersion. Jespersen et al. (2007) proposed the first direct technique to estimate these features using diffusion MRI, with subsequent validation against detailed histology in Jespersen et al. (2010, 2012). Zhang et al. (2012) enabled the *in vivo* mapping of these measures with the development of the neurite orientation dispersion and density imaging (NODDI).

NODDI has had a rapid uptake in the field of neuroimaging as it allows quantification of microstructure changes in both grey matter (GM) and white matter (WM), with a clinically feasible imaging protocol. Clinical studies have been carried out using NODDI for applications including normal brain development and ageing (Chang et al., 2015; Billiet et al., 2015; Nazeri et al., 2015), neurological disorders (Winston et al., 2014; Timmers et al., 2014; Owen et al., 2014; Lemkaddem et al., 2014; Kunz et al., 2014; Eaton-Rosen et al., 2015) and brain connectivity (Lemkaddem et al., 2014). All these studies find that the microstructure specific indices provided by NODDI are clinically relevant. For example, in a study of focal cortical dysplasia, Winston et al. (2014) show that NODDI parameters consistently identify the regions of dysplasia more conspicuously, compared to the changes observed from other MRI modalities. Kunz et al. (2014) use NODDI to assess brain development and show that its indices capture the specific features of the microstructure that change in the major WM pathways

* Corresponding author.
E-mail address: maira.tariq.11@ucl.ac.uk (M. Tariq).

http://dx.doi.org/10.1016/j.neuroimage.2016.01.046

during brain development, including fibre density, myelination and orientation distribution of neurites. Lemkaddem et al. (2014) demonstrate the use of NODDI in connectivity studies and show that the alteration of brain networks in temporal lobe epilepsy are a result of changes in neurite density and orientation dispersion, quantified by NODDI.

Despite its rapid adoption in neuroimaging, a key limitation of NODDI is that it cannot accurately model complex neurite configurations such as those arising from fanning and bending axons. In such fibre configurations, the dispersion about the dominant orientation is the highest in the plane of fanning and bending but the lowest in the plane perpendicular to it, giving rise to anisotropic dispersion, as illustrated in Fig. 1. Anisotropic orientation dispersion is widespread in the brain, as shown by the abundance of fanning/bending fibres in histological brain data (Türe et al., 2000; Kleinnijenhuis et al., 2013; Budde and Annese, 2013) and diffusion MRI studies (Lazar et al., 2005; Sotiropoulos et al., 2012). However, a quantification of such anisotropyhas not been demonstrated *in vivo* and cannot be determined with NODDI, which in its current form only models isotropic orientation dispersion. A measure of anisotropic orientation dispersion of neurites can highlight subtle changes in neurite morphology, which may not alter the overall dispersion. Thus, quantification of anisotropic dispersion will not only provide a more comprehensive description of the orientation dispersion of neurites but may also serve as a marker of subtle microstructural changes in pathology (Lazar et al., 2005) and enhance tractography (Lazar et al., 2005; Rowe et al., 2013).

The aim of this work is to extend the NODDI formalism to enable the characterisation of anisotropic orientation dispersion. To achieve this, we incorporate the Bingham distribution (Bingham, 1974; Fisher et al., 1987) as the orientation distribution function (ODF) in NODDI, instead of the Watson distribution. We quantify anisotropic orientation dispersion of the neurites in terms of the principal components of the Bingham distribution, which describe the extent of orientation dispersion about the dominant orientation, separately along the primary and secondary dispersion orientations. We present indices derived from the parameters of the Bingham distribution to quantify anisotropic orientation dispersion, along with the standard NODDI indices of neurite morphology. The novel indices of Bingham–NODDI allow us to distinguish the changes in overall dispersion from dispersion anisotropy. Hereafter the proposed model will be referred to as Bingham–NODDI, and the original model as Watson–NODDI, owing to the function used to characterise the orientation distribution of neurites.

To evaluate the Bingham–NODDI model, we establish the *in vivo* feasibility of estimating its parameters, specifically the novel indices quantifying anisotropic dispersion. We use synthetic and *in vivo* data to assess the accuracy and precision of estimating the Bingham–NODDI measures, using various single and multi-shell HARDI protocols, including the two-shell NODDI protocol proposed in Zhang et al. (2012). We assess if the new model explains the data better without overfitting by comparing the quality of fit of the Bingham–NODDI and Watson–NODDI models. We also assess whether estimates of any of the NODDI parameters are biased in the presence of dispersion anisotropy when using Watson distribution as a model for the ODF of neurites.

The rest of the paper is organised as follows: the next section presents the Bingham–NODDI model, including a description of the Bingham distribution and the indices, derived to quantify anisotropic orientation dispersion, while the Materials and methods section details the data acquired for synthetic and *in vivo* assessment of these indices. The Experiments and results section outlines the experiments designed to assess the estimation of Bingham–NODDI indices, followed by the obtained results. In the Discussion section we discuss the implications of the findings and conclude with some future work.

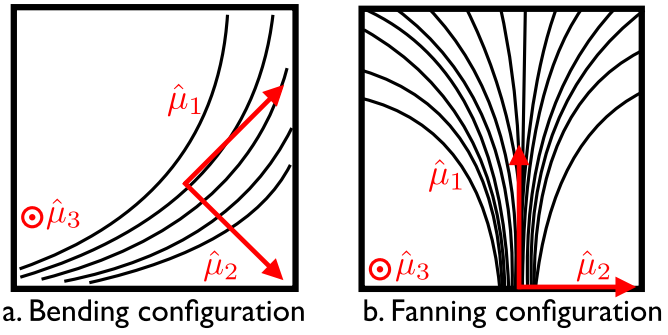

Fig. 1. Schematics illustrating anisotropic orientation dispersion of the fibres in the brain, including bending (a) and fanning (b) of fibres. Such configurations can be interpreted as orientations dispersed about a mean orientation, $\hat{\mu}_1$, with the highest dispersion in the plane of fanning, characterised by $\hat{\mu}_1$ and $\hat{\mu}_2$ and the least in the plane perpendicular to it, defined by $\hat{\mu}_1$ and $\hat{\mu}_3$. The existence of such fibre configurations has been confirmed with histological data. For example, Kleinnijenhuis et al. (2013) show extensive bending/fanning of fibres into the cortex while Budde & Annese (2013) also show sharp bending/fanning of fibres into the cortex, as well as high dispersion in the medial and lateral regions of the corpus callosum (CC). Türe et al. (2000) show the fanning fibres of the corticospinal tracts (CST), as they pass through the internal capsule.

NODDI tissue model

In this section, we describe the tissue model underlying the NODDI framework. In the first subsection, we recap the general NODDI formulation, with particular emphasis on the multi-level compartmentalisation of the NODDI tissue model. The second subsection details the new parameterisation of the ODF to allow estimation of anisotropic orientation dispersion of neurites, followed by a section detailing the implementation of this parameterisation. The last subsection outlines the indices characterising the orientation dispersion of neurites in Bingham–NODDI.

General NODDI formulation

NODDI is underpinned by a two-level multi-compartment model, as shown in Fig. 2, where all compartments are assumed to be non-exchanging. The total normalised signal, A, is modelled as the signal contribution from the tissue and non-tissue components of the brain, weighted by their respective relaxation-weighted volume fractions

$$A = (1 - \nu_{\text{iso}})A_{\text{tissue}} + \nu_{\text{iso}}A_{\text{iso}} \,. \tag{1}$$

The non-tissue compartment represents the free diffusing water in the brain (*e.g.* CSF) and is modelled by free isotropic diffusion, with diffusivity d_{iso}. The volume fraction of this compartment is denoted by ν_{iso} and that of the tissue compartment by $(1\text{-}\nu_{iso})$.

The second level models the signal from tissue compartment, A_{tissue}, comprising the grey and white matter (GM/WM). A_{tissue} is the sum of the signal originating from inside the neurites (intra-neurite) and that from the space outside them (extra-neurite), weighted by their respective volume fractions

$$A_{\text{tissue}} = \nu_{\text{in}}A_{\text{in}} + (1 - \nu_{\text{in}})A_{\text{en}} \,, \tag{2}$$

where A_{in} and A_{en} are the normalised signals from the intra-neurite and extra-neurite compartments, respectively. The intra-neurite volume fraction gives an estimate of the density of neurites and we denote it by ν_{in}, while the extra-neurite volume fraction is $(1\text{-}\nu_{in})$, by construction.

The intra-neurite signal, A_{in}, is computed as the signal from inside a neurite weighted by an orientation distribution function (ODF), $f : \mathbb{S}^2 \rightarrow \mathbb{R}^+$. Neurites are modelled as sticks because in the typical time scale of diffusion MRI experiments, the membrane of neurites restricts the water diffusion to be along their length (Clark et al., 2001). Thus, the diffusion signal from a neurite along an orientation $\hat{n}$ is the attenuation due to this length-wise unhindered diffusion, parallel to the direction of

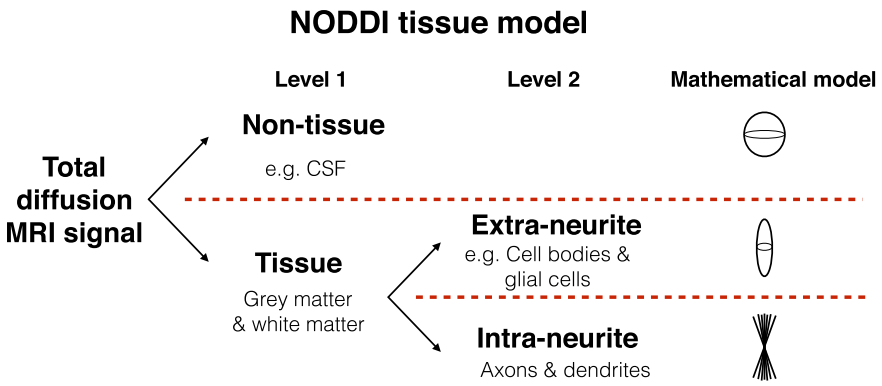

Fig. 2. Breakdown of the total normalised diffusion MRI signal as modelled by NODDI. The contributions of the tissue and non-tissue components of the brain are modelled separately. The tissue signal is further broken down to account for the signal originating from the highly restricted neurites and the hindered space outside the neurites. The non-tissue compartment is modelled by isotropic Gaussian diffusion. The intra-neurite compartment models the neurites as orientationally dispersed sticks, while the space around the neurites is prescribed an anisotropic diffusion model, as detailed in the main text.

applied gradient, *i.e.* $e^{-bd_i(\hat{q}\cdot\hat{n})^2}$. Here b is the diffusion-weighting factor, $\hat{q}$ the gradient direction and d_i the intrinsic diffusivity inside the neurites. To account for the orientational dispersion of neurites, we sum this attenuation over all possible orientations, given a certain density of neurites along each orientation, $\hat{n}$. So

$$A_{in}\int_{\mathbb{S}^2} f(\hat{n})e^{-bd_i(\hat{q}\cdot\hat{n})^2}\mathrm{d}n \ , \tag{3}$$

where $f(\hat{n})\mathrm{d}\hat{n}$ is the probability of neurites with orientations within $d\hat{n}$, an infinitely small cone of orientations centred about $\hat{n}\in\mathbb{S}^2$.

To account for the hindrance due to the presence of neurites, the extra-neurite signal, A_{en}, is modelled as signal attenuation due to anisotropic Gaussian diffusion, *i.e.*

$$A_{\mathrm{en}} = e^{-b\hat{q}^T\mathbf{D}_{\mathrm{en}}\hat{q}} \ , \tag{4}$$

where $\mathbf{D}_{en}$ is the diffusion tensor representing the diffusion characteristics in the extra-neurite space. We model the effect of orientationally dispersed neurites on A_{en} by taking into account the following two observations: a) the dispersion of neurites has an effect on the diffusion in the extra-neurite space, with the diffusion perpendicular to the dominant orientation of neurites being greater if they have high dispersion, b) neurites hinder the diffusion in the surrounding space and this hindrance is greater if the neurite density in that space is greater. The observation a) implies that the extra- and intra-neurite spaces are coupled by the orientation distribution of neurites, $f(\hat{n})$. Thus

$$\mathbf{D}_{en} = \int_{\mathbb{S}^2} f(\hat{n})\mathbf{D}(\hat{n})\mathrm{d}n \tag{5}$$

represents the diffusion tensor in the extra-neurite space in the presence of orientationally dispersed neurites, where $\mathbf{D}(\hat{n})$ is a cylindrically symmetric tensor, with principal diffusion orientation $\hat{n}$, parallel diffusivity $d_\parallel$ and perpendicular diffusivity, $d_\perp$. $\mathbf{D}(\hat{n})$ represents the canonical configuration of perfectly parallel neurites along $\hat{n}$. We assume that for the canonical configuration modelled by $\mathbf{D}(\hat{n})$, the parallel diffusivity in the extra-neurite space is the same as the intrinsic diffusivity inside neurites, *i.e.* $d_i = d_\parallel$. To account for b), a tortuosity model (Szafer et al., 1995) is used to estimate $d_\perp$, for a given neurite density. Thus $d_\perp = d_\parallel(1-\nu_{in})$.

Note that due to the multi-level compartmentalisation of NODDI, when $\nu_{iso}\approx 1$, the tissue parameters describing the intra- and extra-neurite signals can take any value without affecting the total signal (see Eq. (1)). Thus, the tissue parameters are indeterminate for such cases.

Capturing anisotropic dispersion with the Bingham distribution

NODDI in its current form is limited as the orientation distribution of neurites is modelled using the Watson distribution (Mardia & Jupp, 1990), which constrains the dispersion about the dominant orientation, $\hat{\mu}_1$, to be isotropic (Fig. 3a). Here, we utilise the Bingham distribution to quantify the orientation distribution of neurites. As shown in Fig. 3, the Bingham distribution allows us to capture anisotropic orientation dispersion of varying levels, as well as isotropic dispersion, since Watson is a special case of the Bingham distribution.

The Bingham distribution

The Bingham distribution (Bingham, 1974; Fisher et al., 1987) is a parametric orientation distribution, which is the spherical analogue of a two-dimensional Gaussian distribution. The probability density of an orientation along $\hat{n}$ for the Bingham distribution is defined in terms of a 3×3 symmetric matrix, $\mathbf{B}$

$$f(\hat{n};\mathbf{B}) = \frac{1}{c_B}\exp\left(\hat{n}^\top\mathbf{B}\hat{n}\right). \tag{6}$$

Since $f(\hat{n};\mathbf{B})$ is a probability density function, the condition

$$\int_{\mathbb{S}^2} f(\hat{n};\mathbf{B})\ \mathrm{d}\hat{n} = 1 \tag{7}$$

is satisfied, and c_B, the normalisation constant is determined by

$$c_B = {}_1F^1{}_1\left(\frac{1}{2};\frac{3}{2}\mathbf{B}\right) \ , \tag{8}$$

where ${}_1F_1$ is the confluent hypergeometric function of the first kind.

We can obtain a geometrically interpretable form of the Bingham distribution by expressing $\mathbf{B}$ in terms of its eigendecomposition

$$\mathbf{B} = \mathbf{QDQ}^{-1} = (\hat{\mu}_1\ \hat{\mu}_2\ \hat{\mu}_3)\begin{pmatrix}\kappa_1 & 0 & 0\\ 0 & \kappa_2 & 0\\ 0 & 0 & \kappa_3\end{pmatrix}\begin{pmatrix}\hat{\mu}_1^\top\\ \hat{\mu}_2^\top\\ \hat{\mu}_3^\top\end{pmatrix}, \tag{9}$$

such that the diagonal terms reflect the concentrations about the principal axes, $\hat{\mu}_1, \hat{\mu}_2$ and $\hat{\mu}_3$. Here $\mathbf{Q}$ and $\mathbf{D}$ are the matrices of eigenvectors and eigenvalues of $\boldsymbol{B}$, respectively, and $\kappa_1\geq\kappa_2\geq\kappa_3$ represent the concentration of orientations along the corresponding principal axes, as shown in Fig. 3. Symmetry of $\mathbf{B}$ implies that $\mathbf{Q}$ is an orthogonal matrix (*i.e.* $\mathbf{Q}^{-1}=\mathbf{Q}^\top$) and $\hat{\mu}_1$, $\hat{\mu}_2$ and $\hat{\mu}_3$ are mutually orthogonal unit vectors

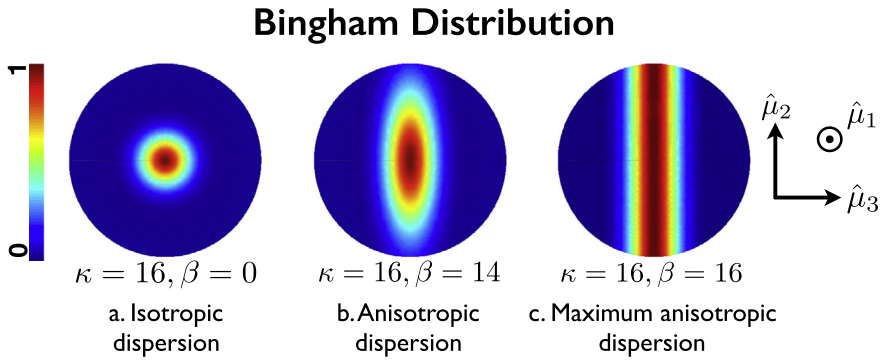

Fig. 3. Probability density plots for the Bingham distribution, which we use to parameterise the orientation dispersion in Bingham–NODDI. The density plots represent increasing anisotropic dispersion about $\hat{\mu}_1$. The primary dispersion orientation, $\hat{\mu}_2$, represents the orientation with the largest dispersion extent about $\hat{\mu}_1$, while $\hat{\mu}_3$ represents that with the least. The vectors $\hat{\mu}_1$, $\hat{\mu}_2$ and $\hat{\mu}_3$ are mutually orthogonal, so $\hat{\mu}_3$ is fixed for a specific $\hat{\mu}_1$ and $\hat{\mu}_2$ (their cross product). Fig. 3a is a special case of the Bingham distribution, where the dispersion is isotropic and is called the *Watson distribution*. (Note that in each of the density plots, the orientation density is normalised with respect to the maximum value and we show the top view of the distribution on a sphere.)

that can be parameterised in terms of Euler's angles, $\theta \in [0,\pi]$, $\phi \in [0,2\pi]$ and $\psi \in [0,\pi]$.

As the Bingham distribution is invariant to addition of arbitrary constants to its eigenvalues (Mardia & Jupp, 1990), by choosing $-\kappa_3$ as the constant, Eq. (6) can be re-written as

$$f(\hat{n};\mathbf{B}) = \frac{1}{c_B}\exp\left(\kappa(\hat{\mu}_1\cdot\hat{n})^2 + \beta(\hat{\mu}_2\cdot\hat{n})^2\right), \tag{10}$$

where $\kappa = \kappa_1 - \kappa_3$ and $\beta = \kappa_2 - \kappa_3$. Bingham distribution thus has only 5 degrees of freedom, two associated with the concentrations and three with the orientations. Thus only two extra parameters need to be determined for the orientation dispersion quantification for Bingham–NODDI compared to Watson–NODDI, namely the concentration parameter β and the angle, ψ.

A more intuitive description of the orientation distribution is achieved by re-writing Eq. (6) in a form that is analogous to the two-dimensional Gaussian distribution

$$f(\hat{n};\mathbf{B}) = \frac{e^{\kappa}}{c_B}\exp\left(-\frac{(\hat{\mu}_2\cdot\hat{n})^2}{1/(\kappa-\beta)}\right)\exp\left(-\frac{(\hat{\mu}_3\cdot\hat{n})^2}{1/\kappa}\right), \tag{11}$$

where $1/(\kappa-\beta)$ and $1/\kappa$ represent the dispersion about the dominant orientation $\hat{\mu}_1$, along the axes $\hat{\mu}_2$ and $\hat{\mu}_3$, respectively (see Appendix A for derivation). These dispersion parameters are analogous to the variance parameters of the Gaussian distribution and inversely proportional to the concentration parameters κ and β. Since $\kappa \geq \beta$, the dispersion along $\hat{\mu}_3$ is less than or equal to that along $\hat{\mu}_2$, as shown in the density plot in Fig. 3. Thus we refer to $\hat{\mu}_2$ as the *primary dispersion orientation*, and $\hat{\mu}_3$ as the *secondary dispersion orientation*.

The estimability of the Bingham distribution and thus the determination of the corresponding orientations and the concentration/dispersion parameters depends on the specific geometry of the underlying orientation distribution of neurites. For the casewhere $\kappa > \beta > 0$, anisotropic dispersion exists about $\hat{\mu}_1$ (Fig. 3b), all the orientations are well-defined and estimable. When the dispersion is isotropic about $\hat{\mu}_1$ (Fig. 3a), the orientations $\hat{\mu}_2$ and $\hat{\mu}_3$ are not distinguishable and thus are arbitrarily defined. Similarly, when the dispersion is completely anisotropic, *i.e.* $\kappa = \beta > 0$ (Fig. 3c), $\hat{\mu}_1$ and $\hat{\mu}_2$ become indistinguishable and arbitrarily defined. For an isotropic orientation distribution ($\kappa = \beta = 0$), none of the orientations is uniquely defined.

Implementation of Bingham–NODDI

In the implementation of Bingham–NODDI, we express the intra- and extra-neurite signals in terms of c_B, the normalisation constant of the Bingham distribution. We compute c_B using the numerical approximation implemented by Koev & Edelman (2006).

To compute A_{in}, we substitute Eq. (6) into Eq. (3), and following some manipulation, get

$$A_{in} = \frac{c_Q}{c_B} = \frac{{}_1F_1\left(\frac{1}{2};\frac{3}{2};\mathbf{Q}\right)}{{}_1F_1\left(\frac{1}{2};\frac{3}{2};\mathbf{B}\right)}, \tag{12}$$

an expression similar to Kaden et al. (2007) and Sotiropoulos et al. (2012). Here c_Q is the normalisation constant for the Bingham distribution, for which the matrix $\mathbf{Q} = \mathbf{B} - bd_i\hat{q}\hat{q}^T$.

To compute A_{en} we substitute Eq. (6) into Eq. (5) to express $\mathbf{D}_{en}$ in terms of the parameters of the Bingham distribution. $\mathbf{D}_{en}$ can be expressed in terms of its eigenvalues and eigenvectors as

$$\mathbf{D}_{en} = \begin{pmatrix}\hat{\mu}_1 & \hat{\mu}_2 & \hat{\mu}_3\end{pmatrix}\begin{pmatrix} d_{\hat{\mu}_1} & 0 & 0 \\ 0 & d_{\hat{\mu}_2} & 0 \\ 0 & 0 & d_{\hat{\mu}_3}\end{pmatrix}\begin{pmatrix}\hat{\mu}_1^{\top} \\ \hat{\mu}_2^{\top} \\ \hat{\mu}_3^{\top}\end{pmatrix}, \tag{13}$$

where $d_{\hat{\mu}_n}$ represents the diffusivity along the nth eigenvector of $\mathbf{D}_{en}$. It can be shown that the diffusivities along the principal eigenvectors of $\mathbf{D}_{en}$ can be obtained by taking the partial derivative of c_B with respect to the corresponding concentration parameter

$$d_{\hat{\mu}_1} = d_\perp + (d_\parallel - d_\perp)\frac{\partial c_B}{\partial \kappa}, \tag{14}$$

$$d_{\hat{\mu}_2} = d_\perp + (d_\parallel - d_\perp)\frac{\partial c_B}{\partial \beta}. \tag{15}$$

We compute these derivatives numerically, using finite differences. The diffusivity along $\hat{\mu}_3$ is then

$$d_{\hat{\mu}_3} = d_\parallel + 2d_\perp - d_{\hat{\mu}_1} - d_{\hat{\mu}_2}, \tag{16}$$

using the fact that $\mathrm{Tr}(\mathbf{D}_{en}) = \mathrm{Tr}(\mathbf{D}(\hat{n})) = d_\parallel + 2d_\perp$.

Dispersion indices of Bingham–NODDI

We quantify the dispersion characteristics of neurites using Bingham–NODDI, by generalising the orientation dispersion index (ODI)

for Watson–NODDI (Zhang et al., 2012). We quantify the dispersion extent along $\hat{\mu}_2$ with the parameter

$$ODI_P = \frac{2}{\pi}\arctan\left(\frac{1}{\kappa-\beta}\right), \tag{17}$$

and that along $\hat{\mu}_3$ with

$$ODI_S = \frac{2}{\pi}\arctan\left(\frac{1}{\kappa-\beta}\right). \tag{18}$$

In the case of Watson distribution (Fig. 3a), where $\beta=0$, ODI_P and ODI_S are equal and reduce to ODI.

Table 1 summarises how these dispersion indices vary for a few configurations of the ODF, including the three configurations shown in the density plots in Fig. 3. As the value of β is increased for the same κ, resulting in an increase in anisotropic dispersion, ODI_P increases while ODI_S remains constant. Thus, while their absolute values indicate the level of dispersion, the relative values of ODI_P and ODI_S are an indicator of dispersion anisotropy. The dispersion characteristics can also be represented in terms of the dispersion angles, α_P and α_S, quantifying the angle associated with the spread along $\hat{\mu}_2$ and $\hat{\mu}_3$ (see Table 1). Quantification of dispersion in terms of dispersion angles is valuable as it allows comparison of different ODFs, independent of their parameterisation.

An alternative representation of an ODF, with anisotropic orientation dispersion, is by describing it using the orthogonal measures of the overall dispersion and dispersion anisotropy. These enable separate quantification of the level of dispersion and that of anisotropic dispersion unlike ODI_P and ODI_S. These measures are described in the following sections.

Overall dispersion index

To estimate the overall orientation dispersion, we observe that the overall spread or dispersion of a multivariate normal distribution can be quantified as the determinant of its covariance matrix. Thus, we propose to estimate the total dispersion by

$$|\Sigma_{Bing}| = \sqrt{\left(\frac{1}{\kappa-\beta}\right)\left(\frac{1}{\kappa}\right)}, \tag{19}$$

which can be mapped to a finite range, similar to ODI_P and ODI_S, giving a measure of total dispersion

$$ODI_{Tot} = \frac{2}{\pi}\arctan\left(|\Sigma_{Bing}|\right). \tag{20}$$

For Watson distribution, the overall orientation dispersion reduces desirably again to ODI. Thus for isotropic dispersion, the ODF can be completely parameterised by a single dispersion index, as done in Zhang et al. (2012). ODI_{Tot} reflects the level of overall dispersion and as shown in Table 1, it increases with increasing ODI_P or ODI_S (decreasing κ or increasing β).

Dispersion anisotropy index

We propose to measure the dispersion anisotropy of neurites with Bingham–NODDI using the index

$$DA_B = \frac{2}{\pi}\arctan\left(\frac{\beta}{\kappa-\beta}\right), \tag{21}$$

which has the value of 0 when $\beta=0$ (isotropic dispersion) and 1 when $\kappa=\beta$, regardless of the actual magnitude of κ and β. DA_B provides a measure sensitive to changes in anisotropic dispersion, which may not change the overall dispersion. Thus DA_B is a useful measure to quantify the anisotropy, even in the WM tracts as coherent as the CC, which bends sharply.

It's worthwhile to compare how DA_B differs from the dispersion anisotropy index we proposed earlier in Tariq et al. (2014), which utilises the planarity measure (Westin et al., 2002) of the *orientation tensor*, **T**

$$DA_T = \frac{(\tau_2-\tau_3)}{\tau_1}. \tag{22}$$

T is the second moment of an ODF and τ_1, τ_2 and τ_3 are its eigenvalues, which are functions of κ and β (see Appendix B). DA_T ranges from 0 for isotropic dispersion, to 1 for maximum dispersion anisotropy. Intuitively, DA_T is a product of the overall dispersion, ODI_{Tot} and DA_B. Thus this quantification of anisotropic dispersion assigns lower value to very coherent tracts like the CC, despite differences in the primary and secondary dispersion values.

DA_B is an important measure because it is orthogonal to the overall dispersion measure ODI_{Tot} and quantifies specifically the anisotropy in the orientation dispersion of neurites, unlike DA_T, which is weighted by the overall dispersion.

We can see this from Table 1 where both DA_B and DA_T change with change in dispersion anisotropy, but when κ and β are changed with their ratio remaining the same (for *e.g.* $\kappa=4,\beta=2$ to $\kappa=16,\beta=8$), DA_B remains constant while DA_T increases. Thus, DA_B reflects purely the dispersion anisotropy about $\hat{\mu}_1$, while DA_T reflects the change in dispersion as well as the anisotropy. Anisotropic dispersion can thus be identified as the difference between ODI_P and ODI_S, but quantified directly by the value of DA_B.

Table 1
The values of the dispersion and dispersion anisotropy indices, corresponding to the various configurations of ODF, specified by the values of κ and β. The dispersion angles are an alternative way to represent the level of dispersion in an ODF and are quantified here as the angles corresponding to 95% spread along $\hat{\mu}_2$ and $\hat{\mu}_3$ and labelled as α_P and α_S, respectively. The configurations corresponding to the density plot in Fig. 3 are highlighted by *.

	ODI_P	ODI_S	ODI_{Tot}	DA_B	DA_T	α_P	α_S
$\kappa=4,\beta=0$	0.16	0.16	0.16	0	0	59.59°	59.59°
$\kappa=4,\beta=2$	0.30	0.16	0.22	0.5	0.19	81.36°	59.59°
$\kappa=4,\beta=4$	1	0.16	1	1	0.73	87.66°	59.59°
*$\kappa=16,\beta=0$	0.04	0.04	0.04	0	0	22.92°	22.92°
$\kappa=16,\beta=8$	0.08	0.04	0.06	0.5	0.04	34.66°	22.92°
*$\kappa=16,\beta=14$	0.30	0.04	0.11	0.91	0.35	81.36°	22.92°
*$\kappa=16,\beta=16$	1	0.04	1	1	0.94	87.66°	22.92°

Materials and methods

In this section, we describe the data acquired for synthetic and *in vivo* assessment of the indices of Bingham–NODDI. We also include details of the model fitting procedure and the preprocessing applied to the data.

In vivo data acquisition

The diffusion MRI data acquired for Zhang et al. (2012) was used in this study, which consists of diffusion MR images of one healthy volunteer (male, 35 years), with informed consent and approval of the local research ethics committee. The *in vivo* images are acquired on a 3T Philips Achieva clinical scanner with $|\boldsymbol{G}|_{\max}=60$ mT/m, using a rich four-shell HARDI protocol, of which the optimised NODDI protocol is a subset. The NODDI protocol consists of two HARDI shells, the first with $b=711$ s/mm^2 and 30 gradient directions and the second with $b=2855$ s/mm^2 and 60 gradient directions, with 9 b = 0 images.[1] The two additional HARDI shells consist of $b=1000$ s/mm^2 and $b=2000$ s/mm^2, with 30 and 60 gradient directions, respectively. The

[1] For a standard scanner with $|\boldsymbol{G}|_{\max}=40$ mT/m, the optimised protocol would consist of reduced b-values of 700 s/mm^2 and 2000 s/mm^2, as discussed in Zhang et al. (2012).

echo time TE = 78 ms and repetition time TR = 12.5 s are the same for all measurements (see Zhang et al., 2012). Different b-values are achieved by varying the gradient strength while holding the diffusion time constant. This minimises the sensitivity of acquired data to axon diameters, making the protocol suitable for our model of zero-radius cylinders for neurites. Isotropic voxels of 2 mm are obtained in 25 min for optimised NODDI protocol, and another 25 min for the additional HARDI shells.

The four-shell protocol is used as a pseudo ground-truth to test the *in vivo* performance of the model, as done in Zhang et al. (2012). We additionally evaluate the parameters estimated for various subsets of the full dataset, to determine whether the Bingham–NODDI indices can be estimated using a reduced orientation sampling scheme. The various combinations of protocols compared are detailed in Table 2.

Table 2
The list of imaging protocols used for evaluation of the parameters estimated. All denotes the complete four-shell protocol, while the rest of the protocols are two-shell (N1, N2 and N3) and single-shell (S1 and S2) subsets of it. The number in brackets denote the number of gradient orientations sampled for each protocol (not including the b = 0 images).

Protocol	Settings
All	Full data set (180)
N1	b = 711 (30) & b = 2855 (60)
N2	b = 711 (15) & b = 2855 (30)
N3	b = 711 (10) & b = 2855 (20)
S1	b = 1000 (30)
S2	b = 2000 (60)

Synthetic data

We synthesise diffusion MR data to obtain signal corresponding to known ground-truth to evaluate the estimated parameters against. Diffusion signal is synthesised using a multi-compartment model as in Zhang et al. (2011), which simulates signals for various neurite densities and diameters while accounting for their orientation dispersion. We substitute the Bingham distribution as the ODF to generate expected diffusion signals in the presence of dispersion anisotropy.

We simulate data for all possible combinations of the set of parameters shown in Table 3, with the restriction $\kappa \geq \beta$ (by definition of the Bingham distribution), to test Bingham–NODDI for various configurations of tissue microstructure expected from the GM and WM in the human brain. We simulate the data for various non-zero axon radii to evaluate the consequence of not modelling the axon radii in Bingham–NODDI. We obtain 250 uniform random rotations of the Bingham distribution, for each tissue configuration, to see if there is any bias in estimates due to the orientational variance of neurites. The random rotations are obtained using the method in Shoemake (1992). Data is synthesised for each of these instantiations (total 180,000) using the four-shell protocol and Rician noise is added with a typical clinical SNR of 20.

Model fitting procedure

The *NODDI* Matlab toolbox[2] is used for fitting the model to the synthetic and *in vivo* data, which provides the maximum likelihood estimates using the two-stage fitting procedure described in Zhang et al. (2012). In the first stage, a crude estimate of the parameters is obtained from a grid of parameters representing typical *in vivo* tissue configurations. In the second stage, the parameters are refined by utilising a Gauss–Newton optimisation scheme, to obtain the maximum likelihood parameters. The toolbox is modified to include the Bingham distribution as the ODF, which uses the numerical implementation proposed by Koev & Edelman (2006), to compute the hypergeometric function in Eq. (8). Diffusivities are fixed to typical values of $d_i = 1.7 \times 10^{-9} m^2 s^{-1}$ and $d_{iso} = 3.0 \times 10^{-9} m^2 s^{-1}$, and it is assumed that $d_{\parallel} = d_i$, as in Zhang et al. (2012). The only explicit constraint in the fitting procedure is applied to κ and β values (≤ 64), for numerical stability of the implementation (Koev & Edelman, 2006). But this is not a practical issue, as it is shown in Zhang et al. (2011) that at very high levels of coherence, the difference in diffusion signal is negligible.

From the estimated parameters of Bingham–NODDI, namely ν_{in}, κ, β, ν_{iso}, S_0, θ, ϕ, ψ, we compute the indices ODI_P, ODI_S, ODI_{Tot}, DA_B and the parameters of $\mathbf{T}$, using the expressions described in Dispersion indices of Bingham-NODDI section. Watson–NODDI is also fitted to the synthetic and *in vivo* datasets for model comparison analysis.

[2] http://nitrc.org/projects/noddi_toolbox

Pre-processing

For *in vivo* data, we manually draw a brain mask to extract the brain parenchyma, using ITK-SNAP (Yushkevich et al., 2006). Only the regions within this mask are used for fitting the models. For a meaningful evaluation of the tissue parameters, we assess the parameters separately for GM and WM regions. For *in vivo* data, the brain parenchyma is segmented using the scheme described in Zhang et al. (2012). For synthetic data, we use the typical values of the parameters for each tissue, as observed in the segmented *in vivo* data.

Experiments and results

This section describes the experiments and presents the results that characterise Bingham–NODDI in terms of its estimability, the choice of acquisition protocol on the estimability, and its performance relative to Watson–NODDI. The evaluation is first performed with synthetic data to understand the characteristics of Bingham–NODDI under idealised conditions. Subsequently, *in vivo* data is used to determine the suitability of Bingham–NODDI for the characterisation of brain tissue microstructure.

Synthetic data experiment

The synthetic data experiment fits the Bingham–NODDI model to the simulated measurements, using known model parameters. The simulated data is obtained as detailed in Synthetic data section, which uses the same parameterisation of the ODF as Bingham–NODDI, but models neurites with non-zero radii. The approach allows us to determine the accuracy and precision of parameter estimation in the most idealised conditions to determine the intrinsic ability to estimate the model parameters, under sampling constraints imposed by the measurement procedure.

Table 3
The ground-truth parameters used to generate the synthetic data. ν_{in} and ν_{iso} represent the intra-neurite and isotropic volume fractions, while κ and β are the concentration parameters of the Bingham distribution. $\hat{\mu}_1$ represents the dominant orientation and $\hat{\mu}_2$ the primary dispersion orientation. α denotes the axon radii.

Parameter	Ground-truth values
ν_{in}	{0.2, 0.4, 0.6, 0.8}
ν_{iso}	{0.0}
α	{0.25, 0.5, 1, 2} μm
κ	{0, 1, 2, 3, 4, 5, 6, 7, 16}
β	{0, 1, 2, 3, 4, 5, 6, 7, 16}
$\hat{\mu}_1$ and $\hat{\mu}_2$	250 uniform random rotations

Parameter estimation

Design

The estimates from Bingham–NODDI fitting to the large set of tissue configurations described in Synthetic data section are used for parameter estimation analysis. For each model parameter, the absolute estimation errors are pooled over instances of the tissue configurations with the same orientation-invariant parameters but different orientations. The mean and the standard deviation of the pooled errors are computed to quantify the accuracy and precision of the model parameters. We show the results for estimation based on the two-shell protocol optimised for Watson–NODDI in Zhang et al. (2012), as it is currently the standard *in vivo* protocol for NODDI. The results for the other protocols (not shown) exhibit similar trends. The parameter estimation with Watson–NODDI fitting is also evaluated to compare with Bingham–NODDI results.

Results for Bingham–NODDI parameters

Fig. 4 summarises the error statistics of estimating the volume fraction parameters. The results show that both parameters can be estimated accurately and precisely (compared to the level of noise) with only a weak dependence on ν_{in}, κ and β. The estimability reduces slightly for lower ν_{in}. This is expected as the reduction in the fraction of restricted diffusion results in increased signal attenuation, which lowers the effective SNR. The weak dependence of the estimability on the concentration parameters reflects the reduced accuracy and precision in estimating large values of κ and β (results not shown). The underestimation of κ and/or β when they take large values is compensated by a slight overestimation of ν_{in}.

Figs. 5 and 6 summarise the error statistics of estimating the orientation dispersion indices of Bingham–NODDI. We find that for most of the plausible neurite configurations, the dispersion indices can be determined accurately and precisely. The results show that the estimability of ODI_P, ODI_S and ODI_{Tot} depends strongly on ν_{in} and the underlying orientation distribution of neurites. The estimation of ODI_P and ODI_{Tot} is also affected by the level of anisotropic dispersion. For all the parameters, the estimability reduces for lower values of ν_{in}, which is expected as reduced ν_{in} means the measured signal has weaker orientation dependence.

The errors and variability for estimation of the dispersion indices are high when the underlying ODF is isotropic. This is expected due to noise induced anisotropy (also seen for the DT in Pierpaoli et al. (1996)),

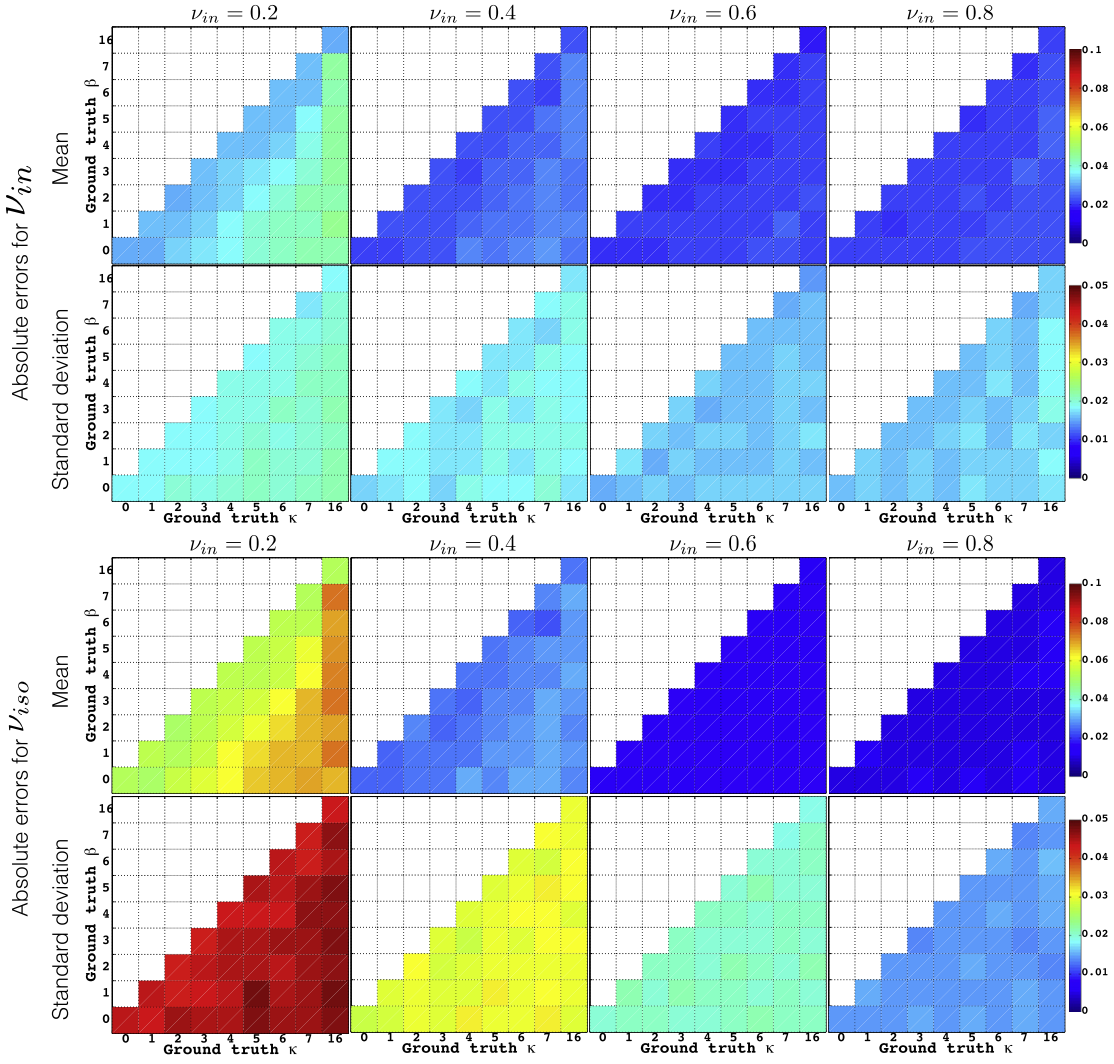

Fig. 4. Statistics of the estimation errors of ν_{in} (top panel) and ν_{iso} (bottom panel) using Bingham–NODDI for the optimised NODDI protocol (N1). Each panel shows the mean (top row) and the standard deviation (bottom row) of the absolute errors. Each column corresponds to the ground-truth value of ν_{in}, as indicated. Each pixel corresponds to one combination of ground-truth κ and β values.

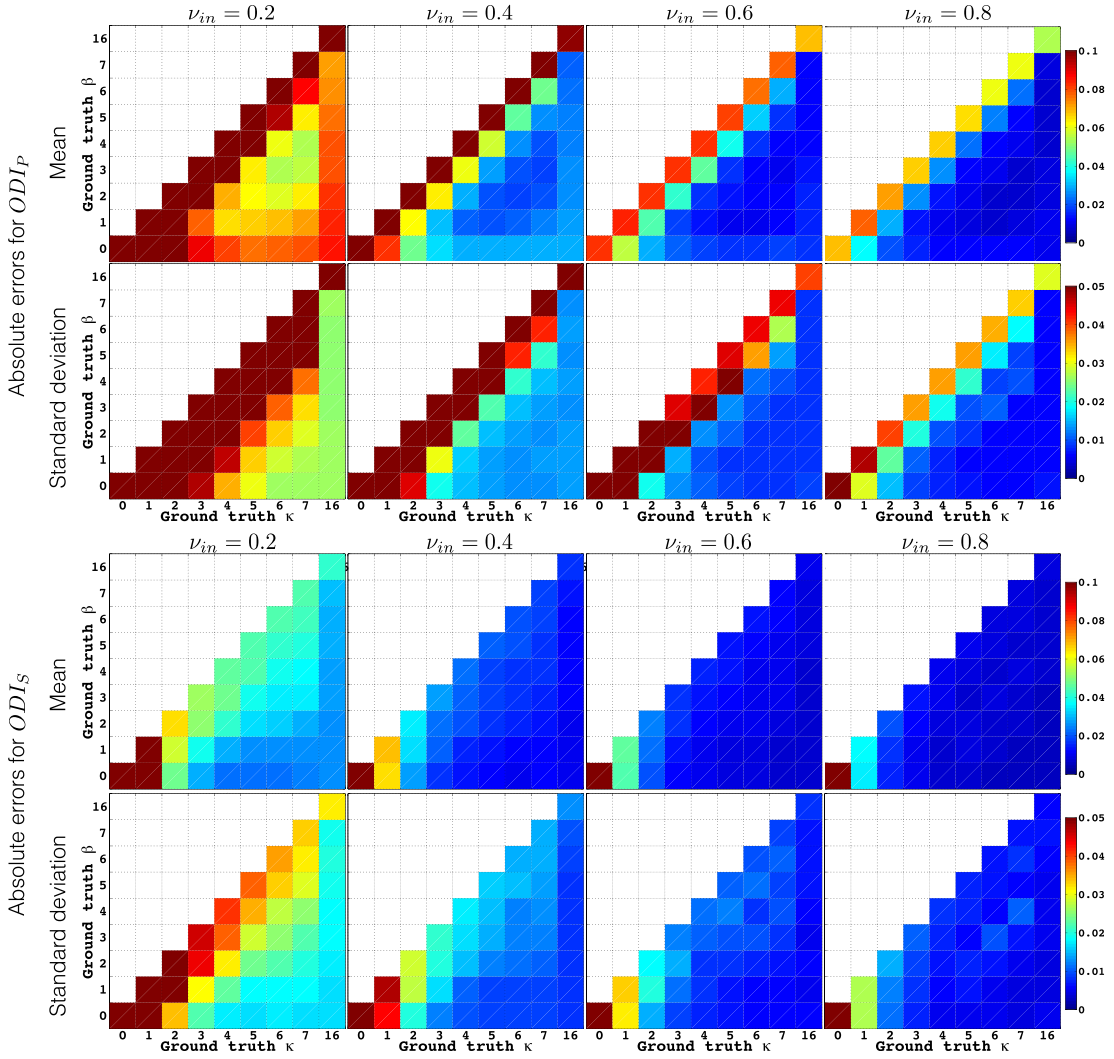

Fig. 5. As Fig. 4 but showing the statistics of estimation errors of ODI_P and ODI_S.

when the underlying ODF is isotropically distributed either about all orientations ($\kappa=0$) or one of the orientations ($\beta=0$ or $\kappa=\beta$). The error and variability are the highest at the corresponding singularities for the specific orientation dispersion index. These findings are consistent with the estimation of *ODI* for Watson–NODDI (Zhang et al., 2012), which was found to be the hardest for the highest level of overall

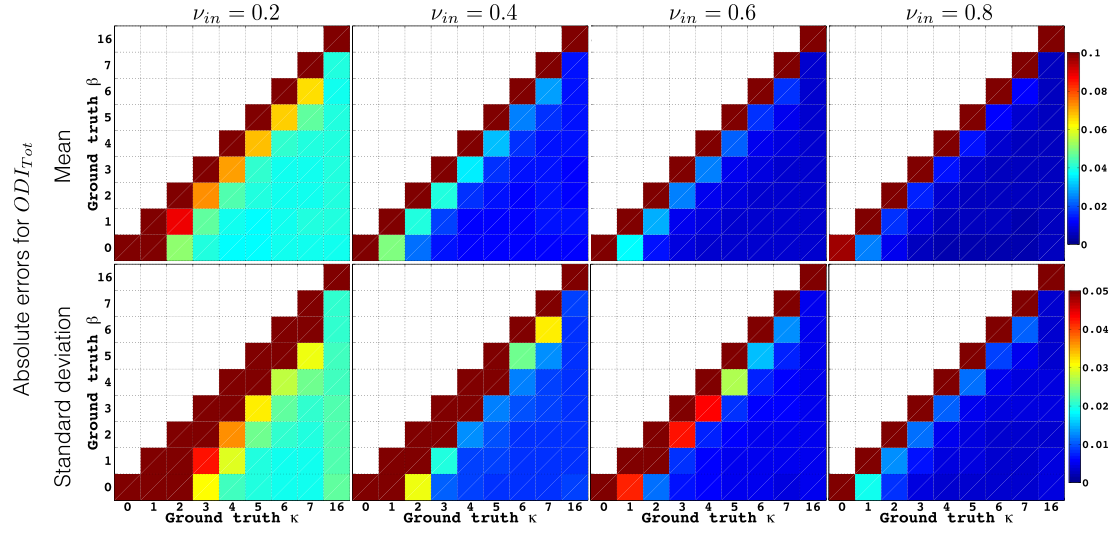

Fig. 6. As Fig. 4 but showing the statistics of estimation errors of ODI_{Tot}.

dispersion (corresponds to $\kappa=0$, where all dispersion parameters are hard to estimate).

Fig. 7 summarises the estimability of the dispersion anisotropy indices DA_B and DA_T. Our results indicate that dispersion anisotropy is harder to estimate than the other metrics of dispersion, but the estimation errors and variability are still modest. We find that the estimation of the anisotropy parameters also depends strongly on ν_{in}, as well as the underlying ODF. Like the dispersion indices, the estimation of the anisotropy indices is harder when ν_{in} is low, as well as when the ODF is isotropically dispersed. The estimation of DA_B is hardest when $\beta=0$, and for DA_T when $\kappa=\beta$ and $\kappa=0$, which correspond to an isotropic ODF at the singularity for the specific index. The estimation of DA_B is also compromised when κ is high, corresponding to poor estimability of κ and β (results not shown). We note that DA_T has much lower errors and variability than DA_B, which is expected as $\mathbf{T}$ is a second order approximation of the Bingham distribution.

The errors and standard deviations for estimating the orientations $\hat{\mu}_1$ and $\hat{\mu}_2$ are shown in Fig. 8. These errors are quantified as the angles between the estimated and the ground-truth orientations. We find that the orientations of the Bingham distribution can be estimated accurately and precisely, for all configurations for which they are well-defined. For $\hat{\mu}_1$ the bias and variability of the estimates is very low for most combinations of the concentration parameters and is high only when $\kappa=\beta=0$ and $\kappa=\beta>0$, i.e. for configurations where $\hat{\mu}_1$ is not well defined (see Fig. 3c). The estimation of $\hat{\mu}_2$ is more variable, especially for very low ν_{in}. The configurations where the errors and variability are consistently high are also the ones where $\hat{\mu}_2$ is not well defined i.e. $\kappa=\beta=0$, $\kappa=\beta>0$ (Fig. 3c) and when $\beta=0$ (Fig. 3a). Increasing ν_{in} reduces the errors and variability for estimation of both the orientations, in the regions where they are well-defined.

Results for Watson–NODDI parameters

The interesting finding from the estimability analysis on the Watson–NODDI parameters is that the simplified ODF does not have a significant impact on the estimation of its parameters. The estimability of the volume fractions, overall dispersion and the dominant orientation, estimated from Watson–NODDI, shows very similar errors and variability to those estimated using Bingham–NODDI, with the same trends with respect to the ground-truth ν_{in}, κ and β values. However, for low ν_{in} the estimation of ODI_{Tot} using Watson–NODDI has less variability compared to Bingham–NODDI (comparing Figs. 6 and 9). Thus, Watson–NODDI provides an accurate estimation of the volume fractions, the dominant orientation and the overall dispersion, but we are unable to determine dispersion anisotropy about $\hat{\mu}_1$, or characterise the dispersion extent along $t\mu_2$ and $\hat{\mu}_3$ separately.

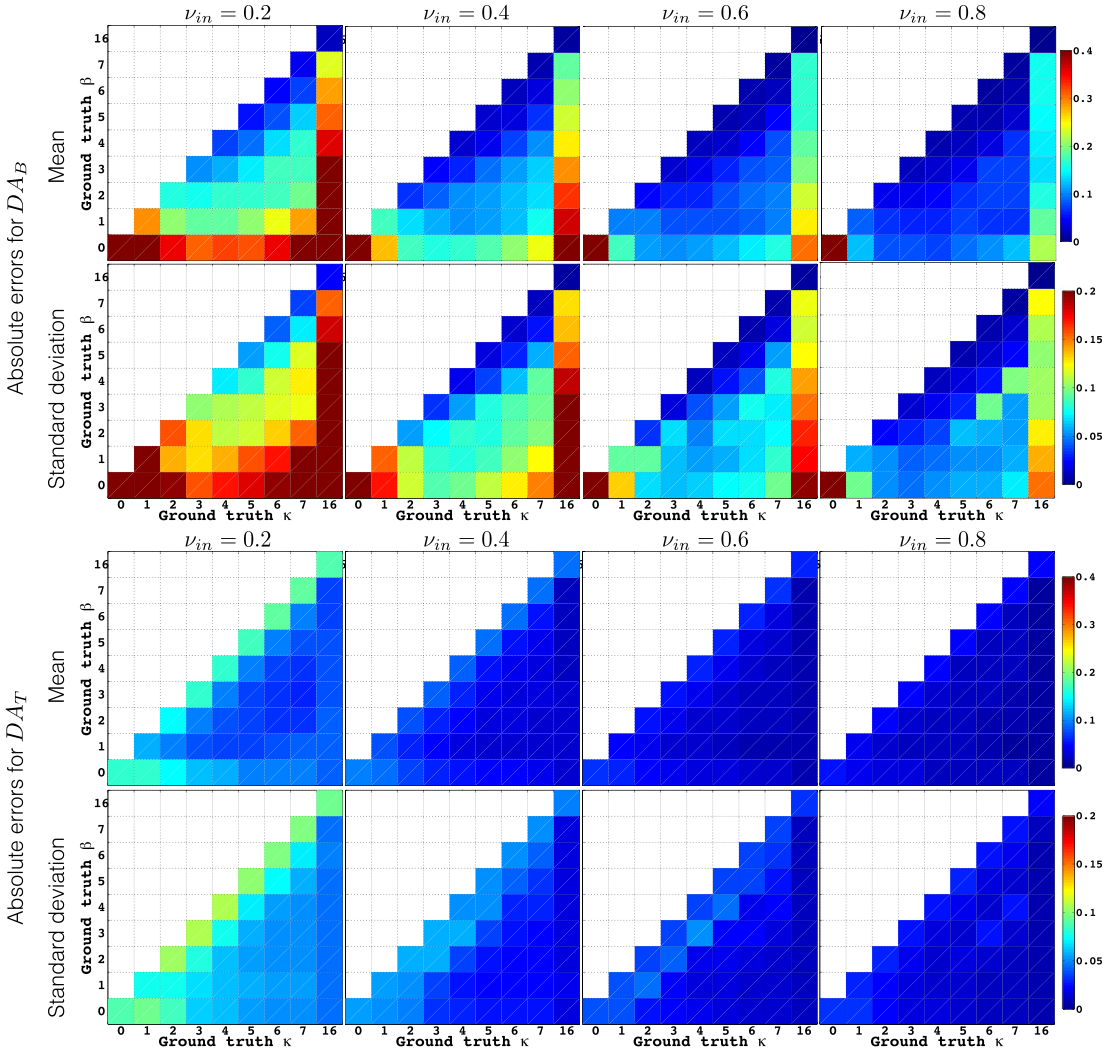

Fig. 7. As Fig. 4 but showing the statistics of estimation errors of DA_B and DA_T.

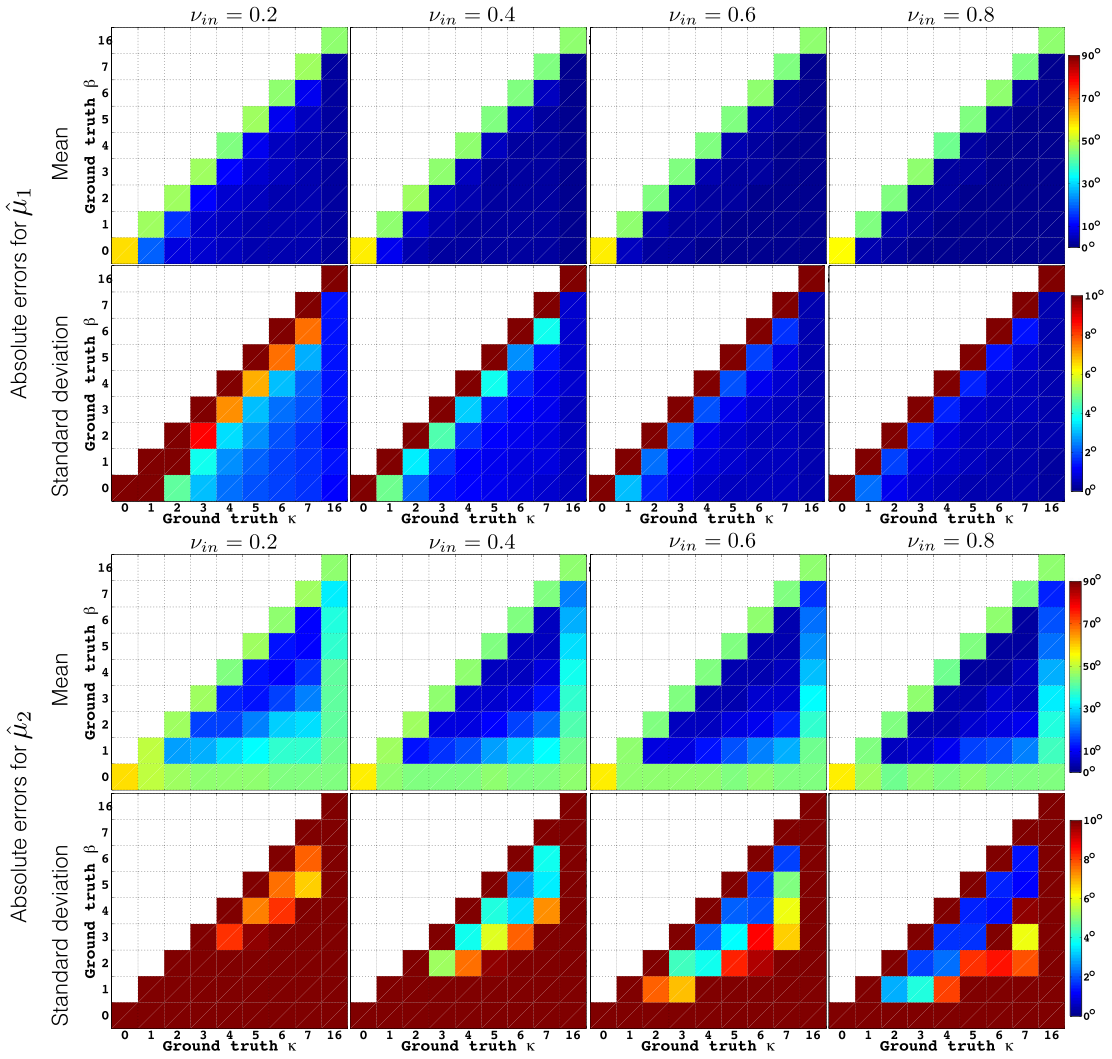

Fig. 8. As Fig. 4 but showing the statistics of estimation errors of $\hat{\mu}_1$ and $\hat{\mu}_2$. The errors correspond to the mean angles between the estimated and the ground truth orientations, for each pool.

Protocol comparison

The aim of the protocol comparison is to assess if it is possible to accurately and precisely estimate the Bingham–NODDI parameters, using the optimised NODDI protocol, N1. We also assess if the acquisition can be further reduced without affecting the quality of estimated parameters, as found true for Watson–NODDI in Zhang et al. (2012). The evaluation of the four-shell protocol is included to determine if

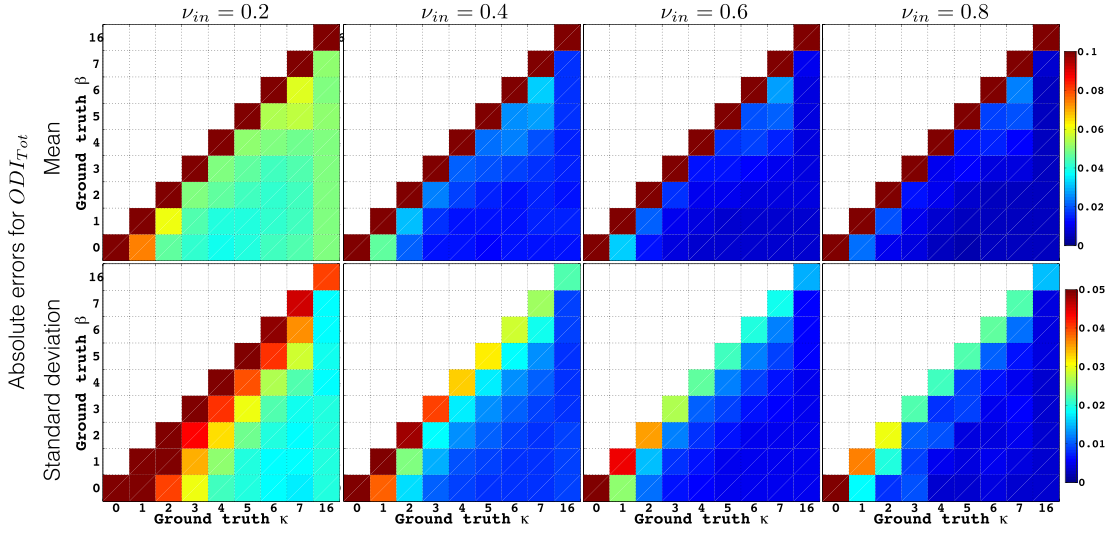

Fig. 9. As Fig. 4 but showing the statistics of estimation errors of ODI_{Tot}, using Watson–NODDI.

using the estimates from this protocol as a pseudo ground-truth for the *in vivo* experiment is a sensible thing to do.

Results

The complete experiment design and the results are included as supplementary material. The results for the estimation of ν_{in} and ν_{iso} are consistent with the findings for the Watson–NODDI (Zhang et al., 2012), namely that a multi-shellprotocol is required to accurately estimate the volume fractions. Estimation of the dispersion indices of Bingham–NODDI follows trends consistent with the Watson–NODDI dispersion index. A single shell with a high b-value is sufficient to estimate the dispersion indices accurately and increasing the number of gradient orientations sampled increases the accuracy of the estimates. The anisotropy measures also have the same trends in protocol comparison as the dispersion indices, but the errors are higher in magnitude. For the orientations, the same trend are seen as for the dispersion indices, except when they are not well defined (Fig. 3c for $\hat{\mu}_1$ and Figs. 3a and c for $\hat{\mu}_2$), where the errors and variability are very high and the protocol used has very little impact on parameter estimation.

In vivo data experiment

Parameter estimation

The aim of parameter estimation analysis is to assess the *in vivo* estimation of the Bingham–NODDI parameters, by looking at the plausibility of the parameter maps and the statistics of parameter estimation.

Parameter maps

We assess whether the parameters of Bingham–NODDI, particularly the novel ones, are sensible in specific tissue regions of the brain. We look at the regions where we expect the dispersion to be highest and lowest, as well as regions where dispersion anisotropy is expected to exist. We show the maps obtained using the estimates from the four-shell protocol.

Results

In Figs. 10 and 11 we see a qualitative analysis of Bingham–NODDI, in the form of the parameter maps of the *in vivo* fitting. The maps demonstrate the *in vivo* feasibility of Bingham–NODDI as we obtain sensible maps of the parameters, which confirm that dispersion anisotropy is widespread in the brain, specifically the peripheral WM. The slices show the cross section of the corpus callosum (CC), corona radiata (CR) (regions in blue in the RGB map, on either sides of the CC), a region known to exhibit fanning as it extends from the internal capsule to the various cortical areas, as well as several peripheral WM tracts.

The RGB maps of $\hat{\mu}_1$ are consistent with the dominant orientations maps expected from DTI fit. The RGB maps are weighted by FA_T, the fractional anisotropy metric for the orientation tensor, $\mathbf{T}$ (Jespersen et al., 2012). The FA_T shows a pattern very similar to *FA* of the DTI, but there are non-negligible intensities even in regions with very high orientation dispersion. The maps of volume fractions representing the intra-neurite and the isotropic compartments are shown in rows 2 and 3 of Fig. 10, which show a spatial pattern consistent with that obtained by fitting Watson–NODDI in Zhang et al. (2012). The maps of the novel dispersion indices ODI_P, ODI_S and ODI_{Tot} (highlighted in yellow in Fig. 10) also show patterns consistent with *ODI* for Watson–NODDI. ODI_P has higher dispersion values throughout the brain tissue, compared to ODI_S, particularly in regions where complex neurites are expected to be present. For example in the CR, as it gets closer to the cortex (see regions of the CR annotated with arrows on slice 26 and 30 in Fig. 10), as well as the tracts near the cortex. This pattern of anisotropy is consistent with findings by Lazar et al. (2005), who use DTI on human data, and Sotiropoulos et al. (2012), who utilise a multi-compartment model similar to Bingham–NODDI, fitted to macaque data. The CC shows low values of ODI_P and ODI_S, as expected.

Dispersion anisotropy is quantified by DA_B and DA_T in Fig. 11. We see high values of dispersion anisotropy indices in various WM tracts, including the CR, the external capsule (EC) and the superior longitudinal fasciculus (SLF), highlighted by arrows in Fig. 11. This is consistent with previous studies exploring the anisotropy of WM tracts in the human brain (Lazar et al., 2005), showing that dispersion anisotropy is a widespread feature of the WM. Since DA_B maps pure anisotropy, even a regions as coherent as the CC has a high values (dashed arrow in Fig. 11), consistent with the known bending of the tract. The higher values in the DA_T map are consistent with DA_B, but there is a greater contrast between the various regions with anisotropic dispersion, depending on whether they have high overall dispersion or not. For e.g. the CC has a lower DA_T compared to regions like the CR. Such a mapping is suited for tractography, where the extent of dispersion is very important to correctly trace streamlines and higher anisotropy significantly change the ODF only when the overall dispersion is high. As expected, DA_B map shows higher variability in estimates compared to DA_T.

Crossing fibres are not explicitly modelled in Bingham–NODDI, but regions of two fibres crossing are also seen to have higher values of DA_B (e.g. the crossing of CR and CC). Regions with three fibres crossing appear to have low DA_B but higher overall dispersion, e.g. where the CR and CC cross the SLF. Examples of crossings between two and three fibre populations are highlighted in Fig. 11.

The primary dispersion orientations, $\hat{\mu}_2$, estimated by Bingham–NODDI (Fig. 11, row 2) match very well with the secondary eigenvalues of the DTI and follow the findings in Lazar et al. (2005). We see some incoherence in the estimation of $\hat{\mu}_2$ in the midsagittal plane. Lazar et al. (2005) suggest that this corresponds to regions of high axial symmetry ($\hat{\mu}_2$ is degenerate in this case). We think it could also be a result of low SNR in the deep-lying brain regions.

Quantitative analysis

We explicitly compare the performance of the *in vivo* estimates obtained from the Bingham–NODDI and Watson–NODDI models, using the statistics of estimation of comparable parameters. This is to evaluate how important it is to model anisotropic dispersion and if modelling for this anisotropy affects the accuracy and precision of the parameters.

Design

We compare the accuracy and precision of the estimates obtained by fitting to data from N1, the standard *in vivo* protocol for NODDI. In particular, we want to quantify the consequence of not including dispersion anisotropy in the NODDI model. Towards this end, we stratify our results according to the level of dispersion anisotropy determined by the value of DA_B. We use the DA_B estimated by fitting the *in vivo* data from the four-shell protocol.

Results

The quantitative comparison of the estimates of the two models reveals that the estimation of ν_{in}, ν_{iso} and $\hat{\mu}_1$ (results not shown) is the same for the two models, regardless of the level of anisotropic dispersion, while the estimation of ODI_{Tot} gets slightly worse for Watson–NODDI for higher levels of dispersion anisotropy (Fig. 12). The Watson–NODDI estimates are overall comparable to Bingham–NODDI ones, as concluded also from the synthetic data experiment, with a slight increase in bias for ODI_{Tot}, specifically notable for GM. Thus, Watson–NODDI is able to reliably estimate the volume fractions, the overall dispersion and the dominant orientation of the neurites, but Bingham–NODDI provides extra information by separately quantifying ODI_P and ODI_S, to enable quantification of anisotropic orientation dispersion.

Model comparison

We compare how well the two models explain the data. We use a standard model selection criterion, the Bayesian Information Criterion,

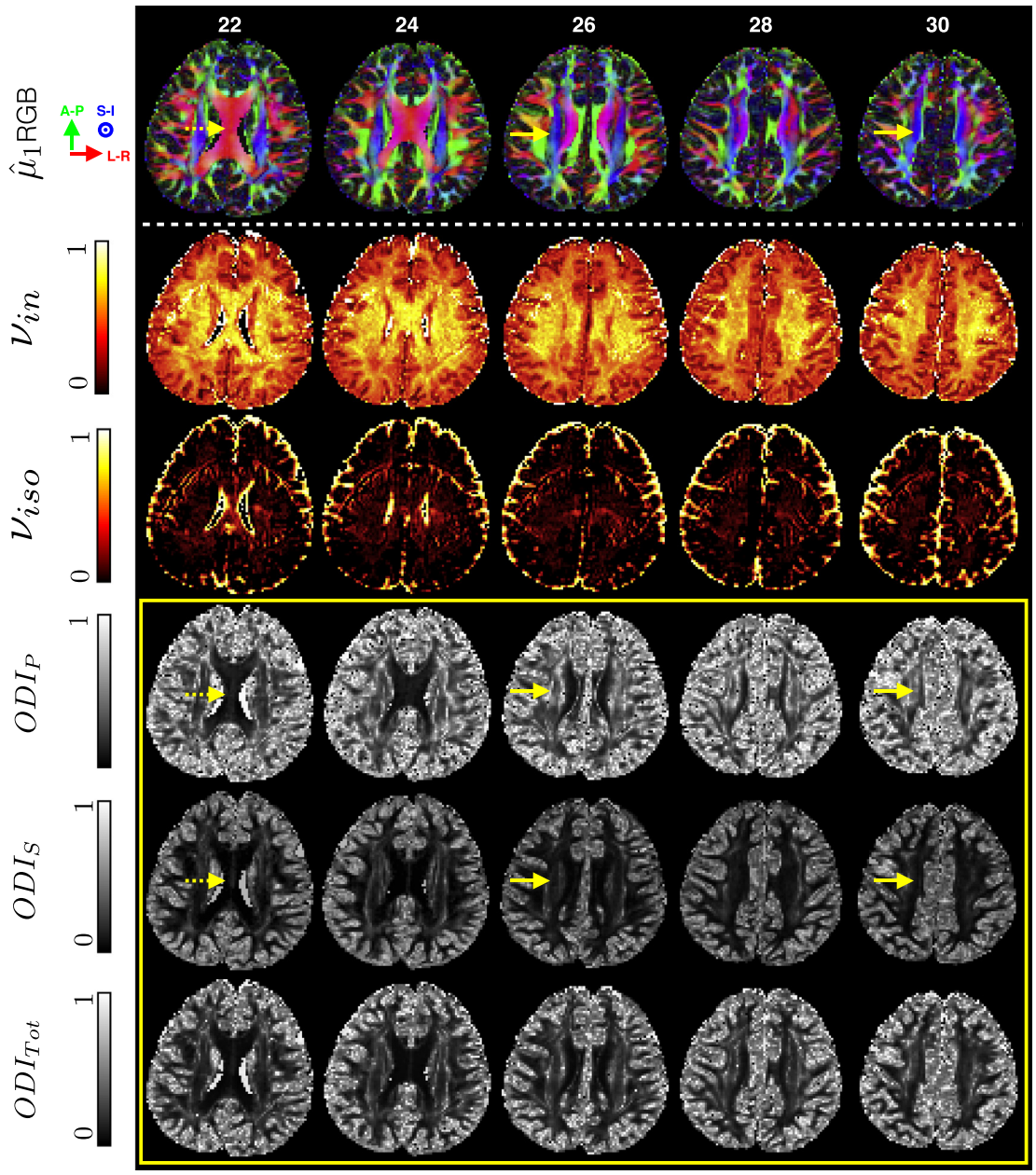

Fig. 10. Axial slices showing maps of the novel parameters ODI_P, ODI_S and ODI_{Tot} (highlighted in yellow), obtained by fitting Bingham–NODDI to the *in vivo* data, along with the estimated ν_{in}, ν_{iso} ($2^{nd}$and 3^{rd} rows). Corresponding RGB maps of dominant orientation ($\hat{\mu}_1$) are shown as anatomical reference (row 1). The RGB maps are weighted by FA_T, the overall anisotropy metric for the orientation tensor, **T** (Jespersen et al., 2012). The dashed arrows indicate the CC, while the solid arrows highlight regions of CR across various slices.

BIC (Schwarz, 1978), which quantifies the quality of fit to the data while accounting for model complexity (number of parameters).

Results

Fig. 13 shows the BIC maps for Bingham–NODDI and Watson–NODDI, where a lower value corresponds to a model which explains the data better. The maps clearly show that Bingham–NODDI explains the data better than Watson–NODDI, in a significant proportion of the voxels. The raw BIC maps (Fig. 13, rows 2 and 3) highlight that Bingham–NODDI is the preferred model in most WM regions, but in GM and the very coherent WM regions (e.g. midsagittal CC) Watson–NODDI is sufficient. The higher BIC values in the Watson–NODDI fit correspond to regions of WM with expected fanning/bending configurations. The maps of difference in BIC values between the two models (Fig. 13, rows 4 and 5) highlight these findings clearly.

Protocol comparison

We carry out a protocol comparison, similar to that for synthetic data, to establish if the Bingham–NODDI parameters can be estimated *in vivo* with the standard NODDI protocol, N1, and if the protocol can be further reduced without impacting the accuracy and precision of the estimates. We compare the obtained results to those for the synthetic data in Protocol comparison section.

Results

The complete experiment design and the results for the protocol comparison are included as supplementary material with this article. We find that all the results for the various protocols are consistent with the findings from the synthetic data experiment and show that the parameters of Bingham–NODDI are estimable with N1 protocol. We notice that for all the parameters, the estimation appears to be

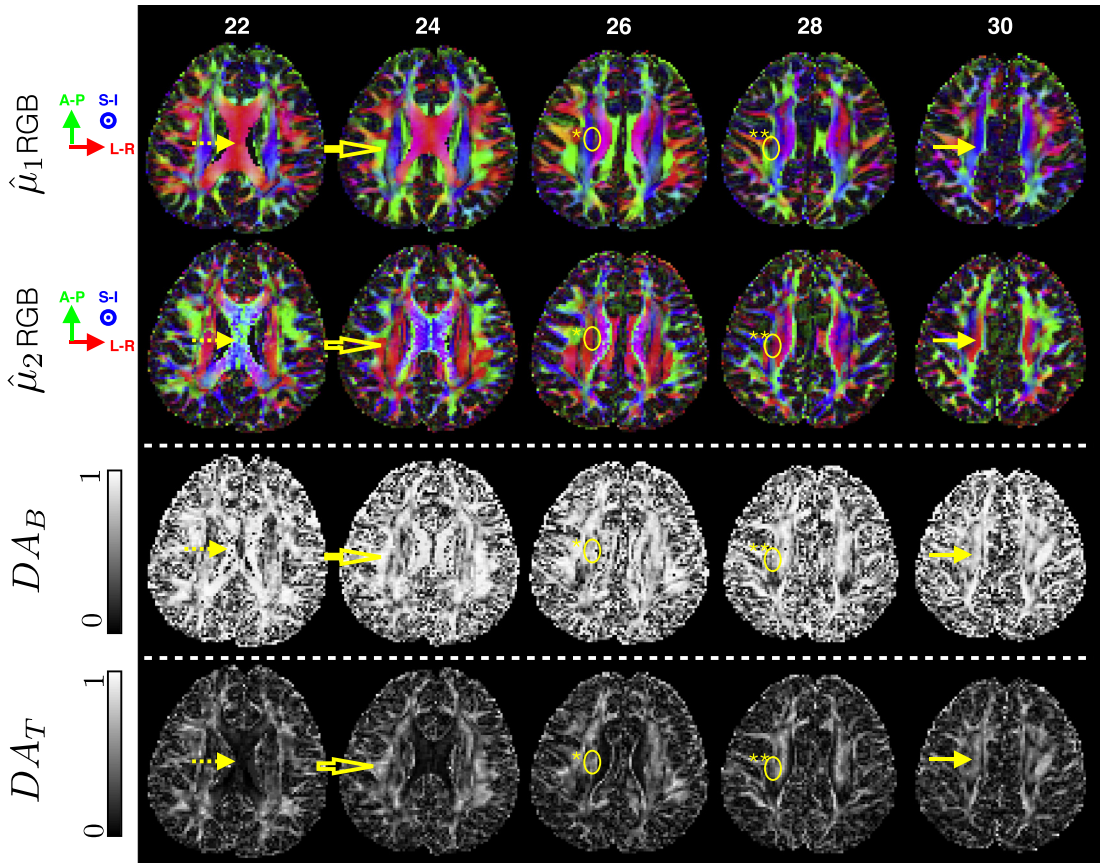

Fig. 11. As Fig. 10, but showing maps of the proposed quantifications of dispersion anisotropy. The RGB maps of $\hat{\mu}_2$ weighted by FA_T are also shown. The dashed arrows indicate the CC, the solid arrows the CR and the un-filled arrows highlight the SLF. Regions of crossings are highlighted with circles, with * indicating a crossing with two fibre populations and ** with three.

more variable for *in vivo* than the synthetic data. This is likely explained by the fact that the NODDI model remains an imperfect representation of the measured data.

Discussion

In this paper we propose Bingham–NODDI, a generalisation of the Watson–NODDI model, to characterise the anisotropic orientation dispersion of neurites, which provides a more accurate representation of the orientation distribution of neurites in the human brain. Anisotropic dispersion is a characteristic of fanning and bending fibres, seen in the histological data of various regions of the brain (Türe et al., 2000; Kleinnijenhuis et al., 2013; Budde & Annese, 2013). Characterisation of anisotropic orientation dispersion is important as it is a widespread feature in the brain (Lazar et al., 2005; Sotiropoulos et al., 2012) and can serve as a useful marker of brain pathologies, reflecting very subtle changes in the orientation dispersion of neurites. It is conceivable that a change in the orientation dispersion of neurites occurs such that there is little or no change in the overall dispersion, but the level of dispersion anisotropy is altered. Watson–NODDI can only estimate the overall

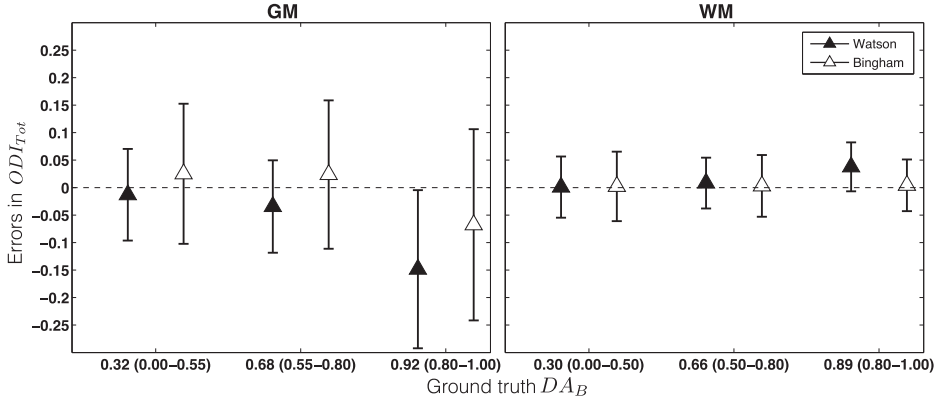

Fig. 12. Errors in estimation of the overall dispersion index, ODI_{Tot} using Bingham–NODDI and Watson–NODDI, for various ground truth values of DA_B, for *in vivo* data. The results are shown for GM and WM, obtained by fitting the two-shell NODDI protocol (N1). The ground-truth values shown are the mean values in each pool, with the range of those values indicated in brackets.

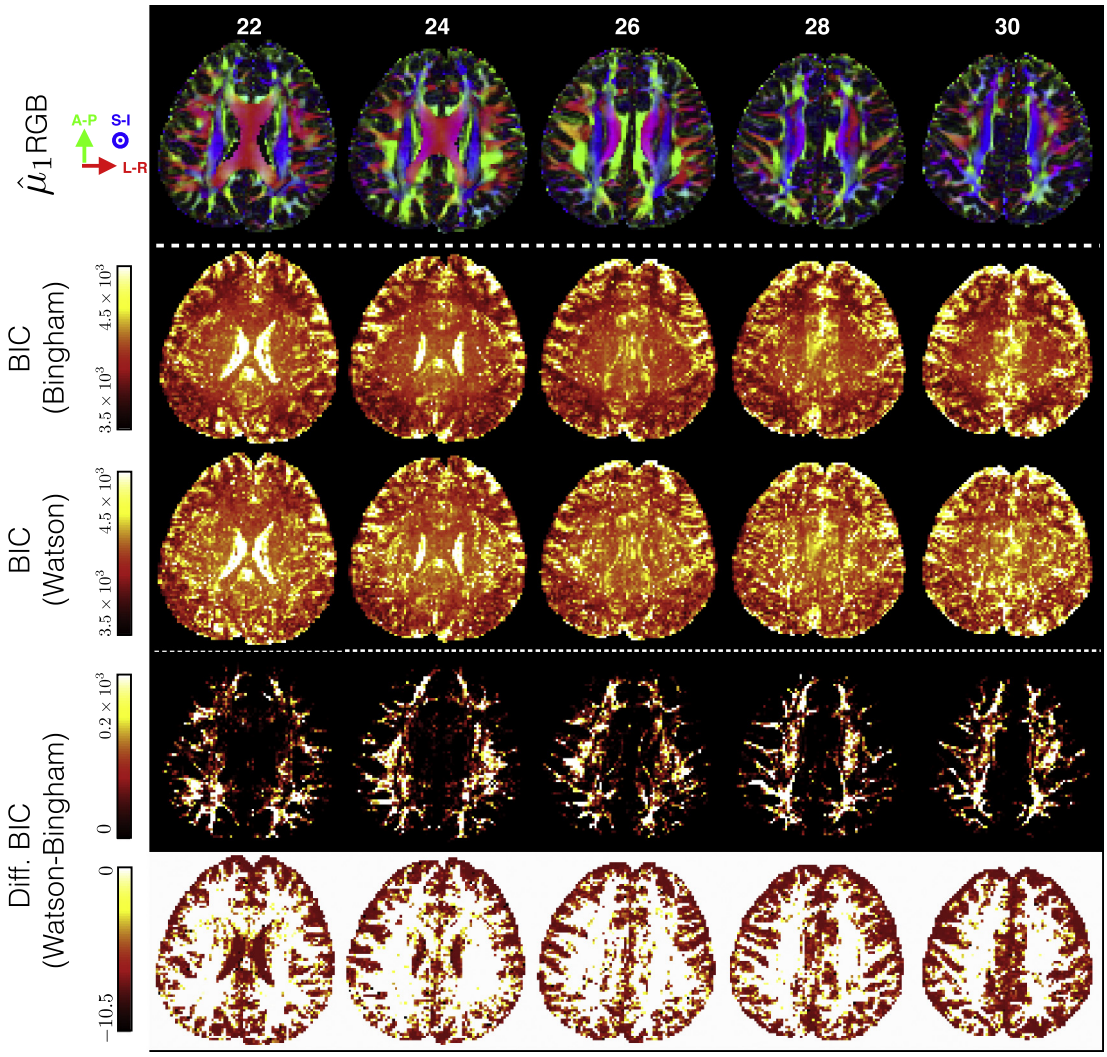

Fig. 13. The maps of BIC for fitting with Bingham–NODDI and Watson–NODDI models (2^{nd} and 3^{rd} rows). The last two rows show the difference BIC maps to highlight the areas where Watson–NODDI performs worse than Bingham–NODDI (4^{th} row) and those where Watson–NODDI is sufficient (5^{th} row). For clarity, the BIC difference map has been modified to show the positive and negative intensities separately. The number of negative values in the difference map corresponds to regions where Watson–NODDI is sufficient, but a small number also represent voxels where the fitting procedure gets stuck in local minima (see discussion in Limitations and future work section).

dispersion and will not be sensitive to such a change while Bingham–NODDI can capture this subtle difference in the orientation distribution.

We include the Bingham distribution as the orientation distribution function in the NODDI model (Zhang et al., 2012), allowing us to derive the parameters to separately quantify the dispersions extent along the primary and secondary dispersion orientations. Thus, we can distinguish the changes in overall dispersion from dispersion anisotropy and independently quantify these with the indices ODI_{Tot} and DA_B, respectively. DA_B is useful as it provides a marker specific to changes in the anisotropy of the orientation dispersion of neurites. However, DA_B is harder to estimate compared to other indices of Bingham–NODDI. An alternative quantification of anisotropy is DA_T, which has utility in tractography and is very robust. However, it is a second order approximation of the ODF and cannot represent higher order variations in the ODF. DA_T is defined for any generic ODF and thus may be utilised to quantify anisotropic dispersion for an alternative parameterisation of the ODF, but DA_B is specifically defined for the Bingham distribution.

Estimation of neurite morphology using Bingham–NODDI

Our results demonstrate the *in vivo* feasibility of the proposed model and show that the model provides sensible estimates of neurite microstructure, with a clinically feasible protocol. The error analysis on the Bingham–NODDI parameters reveals that they have good estimability. The errors and variability of estimates are commensurate with the level of noise in the synthetic and *in vivo* data. Cases, where the errors and standard deviations are high, correspond mostly to degenerate cases (one or more the model parameters are not well defined).

We show that a two-shell HARDI protocol is sufficient to estimate the indices of Bingham–NODDI, as with Watson–NODDI. Thus, the estimation of Bingham–NODDI parameters is possible with a clinically feasible imaging protocol. However, the parameters DA_B and μ_2 are harder to estimate and unlike Watson–NODDI, a reduced-orientation sampling scheme like *N2* and *N3* are not feasible for Bingham–NODDI. Increasing the angular resolution of the acquisition protocol would be expected to make the estimation of these parameters more accurate and reliable, however, the configurations where μ_2 is not well defined, would not become estimable even with a protocol with higher orientation sampling. Obtaining a very high orientation sampling is not yet clinically feasible with existing imaging sequences, but emerging technologies such as multi-band imaging (Feinberg et al., 2010) will make it possible to acquire more data per unit time, enabling higher orientation sampling in the same acquisition time.

Model comparison, with BIC, reveals that Bingham–NODDI is the preferred model in most WM regions of the brain. We significantly improve the fitting in these regions by adding just two parameters to

NODDI, which originally has one less parameter than the standard DTI model. Watson–NODDI is sufficient for most of the GM, which is expected as the dendrites are mostly randomly dispersed, and where dispersion anisotropy does exist (e.g. pyramidal neurons) it might be too minute to be discerned with our data. Follow-on work will investigate this further with the state-of-the-art acquisition, such as the Human Connectome Project (HCP) data. [3]

Interestingly, the accuracy of most of the NODDI parameters is not affected by the simplified ODF model used in Watson–NODDI. This includes the volume fractions v_{in} and v_{iso}, the overall dispersion ODI_{Tot}, as well the dominant orientation μ_1. Thus, any studies which have already been carried out with Watson–NODDI are still valid, but the data may be reanalysed using Bingham–NODDI, to obtain a richer characterisation of orientation dispersion and quantify dispersion anisotropy, without any additional acquisition requirements.

In previous work (Tariq et al., 2014), we explored the quantification of anisotropic orientation dispersion of neurites, in terms of **T**, as described in Dispersion anisotropy index section. The alternative parameters for quantification of dispersion are the coherence parameters τ_1 and τ_2, and DA_T for dispersion anisotropy. The evaluation of estimability of these parameters revealed that they are more reliable compared to the indices of anisotropic dispersion proposed here (results not shown). This is expected as these parameters are derived from the second order approximation of the actual ODF, and thus can provide a useful summary metric for the overall orientation dispersion.

Existing diffusion MRI models using the Bingham distribution

Bingham distribution has been used in various diffusion MRI techniques (Cook et al., 2004; Kaden et al., 2007; Sotiropoulos et al., 2012), but the focus has been on mapping brain connectivity while our aim is to estimate biophysically meaningful parameters. The key distinction in this work over these approaches is the use of multi-shell data, as in Zhang et al. (2012), which enables estimation of microstructure at the same time as the fibre dispersion parameters. This works is the first to present a specific quantification of anisotropic dispersion and provide a thorough evaluation of its estimability, while previous studies only explore the level of dispersion anisotropy, using DTI (Lazar et al., 2005) or multi-compartment models (Kaden et al., 2007; Sotiropoulos et al., 2012), but do not explicitly quantify this feature.

As shown in Lazar et al. (2005), the eigenvalues of the diffusion tensor (DT), specifically the difference $\lambda_2 - \lambda_3$, can be used to reflect the level of dispersion anisotropy in WM tracts. Our results are consistent with their findings and there is no significant difference in the orientations estimated by Bingham–NODDI and the three eigenvalues of the DT. However, the DT and the ODF in Bingham–NODDI represent fundamentally different physical properties. DT represents the diffusion profiles associated with the underlying microstructure and the ODF represents the orientation dispersion pattern of the neurites. Similarly, DA_B and λ_2-λ_3 are fundamentally different. DA_B is specific to the orientation distribution; the latter is influenced by DA_B but also by other features like neurite density. Thus, DA_B will be useful to highlight changes specifically in the dispersion of neurites, as a result of brain injury or disruption to normal brain development, which may not be seen by the DT or its anisotropy measure, as many confounding factors can contribute to changes in the diffusion characteristics.

Limitations and future work

A limitation of the proposed model is not explicitly estimating crossing fibres. Our primary aim is to provide simple and robust indices of microstructure and attempting to resolve multiple fibre populations will introduce instability in parameter estimation as discovered by Sotiropoulos et al. (2012). Nevertheless, we find that the model correctly identifies crossing regions with high orientation dispersion and some with high anisotropic dispersion. We confirm this by synthetic experiment, where we explicitly model crossing fibres, in the presence of dispersion, using the Bingham–NODDI model. We simulate a data with high neurite density ($v_{in} = 0.7$) and coherence ($\kappa = 32$), with no and some dispersion anisotropy ($\beta = [0, 16]$) (results included as supplementary material). We find that as expected, and noted from the *in-vivo* experiments, increasing the crossing angle between the two fibre populations results in an increase in the estimated dispersion and dispersion anisotropy indices. In future, we would like to investigate the possibility of incorporating crossing fibres using Bingham–NODDI. Riffert et al. (2014) estimate the Bingham distribution for each peak of the estimated fibre ODF, avoiding the instability of estimating the mixture of Bingham distributions directly from the data (Sotiropoulos et al., 2012). In future we would like to explore a similar approach, to first estimate the number of fibre populations (using for e.g. constrained spherical deconvolution (CSD) (Tournier et al., 2007)) and then fitting Bingham–NODDI as a mixture of Bingham distributions, with the already estimated orientations, for stable estimates. This will allow estimation of microstructure specific indices while accounting for the existence of both crossings and anisotropic orientation dispersion.

In the presented results, the diffusivity of the intra-neurite and the CSF compartments are fixed to typical values, and the intrinsic diffusivity is assumed to be the same in all tissue compartments ($d_i = d_\parallel$), as with the original model (Zhang et al., 2012). This enables us to obtain robust estimates of tissue microstructure with a clinical imaging protocol. However, this can introduce a bias to the estimated parameters as discussed by Jelescu et al. (2015). This may not be a practical concern as the estimates made with these assumptions correlate well with histology, as shown by Kleinnijenhuis et al. (2013). In future, such assumptions could be relaxed, with more efficient imaging acquisition protocols (Feinberg et al., 2010).

The acquisition protocols used to evaluate Bingham–NODDI are the ones used in the original paper (Zhang et al., 2012) and the two-shell protocol optimised for Watson–NODDI performs the best. However, it will be beneficial to carry out a protocol optimisation procedure specifically for Bingham–NODDI. This will enable us to determine the specific protocol required to reliably estimate the parameters of Bingham–NODDI, specifically the ones that are harder to estimate.

The computational efficiency of the current model fitting implementation is a concern. The NODDI Matlab toolbox takes approximately 60 hours to fit the whole brain data used here. This can be addressed with the convex optimisation procedure proposed by Daducci et al. (2015), which converts the non-linear fitting into a linear optimisation problem, dramatically reducing the processing speed. A preliminary work extends this framework to allow robust estimation of multiple fibre populations, as well as microstructure indices (Auria et al., 2015).

The fitting procedure used here may not be optimal for fitting Bingham–NODDI. We find that for a small but non-negligible number of the voxels, the objective function indicates that Watson–NODDI fits the data better than Bingham–NODDI, corresponding mainly to the regions of partial volume between GM or WM and CSF. As Bingham–NODDI should fit the data at least as well as Watson–NODDI, this indicates that our fitting procedure is getting stuck in local minima for these voxels. We can improve the fitting procedure in these regions by using the Watson–NODDI fit as the starting point for Bingham–NODDI. Future work will thus focus on establishing the optimum fitting procedure for Bingham–NODDI.

To show the clinical utility of the Bingham–NODDI metrics, we need to carry out a clinical study using the model. Such a study will be beneficial in determining how specific the indices are to a certain pathology and thus how useful the model is in practise. This will also help to evaluate if including the Bingham distribution, a more complex model for the ODF of neurites, improves the diagnosis and/or prognosis of the

[3] Available online at http://www.humanconnectomeproject.org/data/

disease, compared to Watson–NODDI. This can also reveal how useful ODI_P, ODI_S and DA_B are compared to the corresponding indices derived from the second order approximation of the ODF, which are more robust to noise. We find the errors and variability of the Bingham–NODDI metrics to be moderate, but a clinical study will help determine if they can distinguish normal and pathological tissue, and thus show how reasonable the statistics of estimation are in practise.

To validate the indices of Bingham–NODDI, we can utilise the histological data used in Kleinnijenhuis et al. (2013). This will build on the preliminary work in Tariq et al. (2015), which shows plausible values of Bingham–NODDI indices in the human neocortex. The validation study will aim to provide a thorough analysis of the estimated parameters from Bingham–NODDI and how accurately they describe the underlying microstructure.

Acknowledgments

MT is supported by the EPSRC (EP/K502959/1) and the EPSRC Centre for Doctoral Training (EP/L016478/1). HZ and DCA are supported by the EPSRC (EP/L022680/1) and the MRC (MR/L011530/1). HZ is additionally supported by the Royal Academy of Engineering Research Exchanges with India and the Royal Society International Exchange Scheme with China.

The NMR research unit (CWK) is supported by a programme grant from the UK MS Society (grant 892/08), which funds the 3T scanner, and the Department of Health's National Institute for Health Research Biomedical Research Centres (BRC), which funds the infrastructure (Capital Project Number R&D03/10/RAG0449). CWK has also received funding from the Engineering and Physical Sciences Research Council (EPSRC) (grant P/I027084/01).

We would also like to thank our anonymous reviewers for providing invaluable feedback on our manuscript, which has led to significant improvement of this manuscript.

Appendix A. Bingham, a spherical analogue of the 2D Gaussian distribution

Bingham distribution is the spherical analogue of a 2D Gaussian probability density function. We draw on this observation to derive Eq. (11) in The Bingham distribution section, as we demonstrate below.

A 2D Gaussian distribution represents the probability of a random variable, $\vec{x}$ as

$$f\left(\vec{x};\sum\right)=c_G\ \exp\left(-\frac{\left(\vec{x}-\vec{\mu}\right)^T\sum^{-1}\left(\vec{x}-\vec{\mu}\right)}{2}\right), \tag{A.1}$$

where $\vec{\mu}=\begin{pmatrix}\mu_1\\ \mu_2\end{pmatrix}$ is the mean and $\Sigma=\sigma_1{}^2\hat{e}_1\hat{e}_1{}^\top+\sigma_2{}^2\hat{e}_2\hat{e}_2{}^\top$ the variance of the distribution, expressed in terms of σ_i and $\hat{e}_i$, which represent the i-th eigenvalue and eigenvector of the distribution. This expression can be simplified to

$$f\left(\vec{x};\sum\right)=c_G\ \exp\left(-\left[\frac{\hat{e}_1\cdot\left(\vec{x}-\vec{\mu}\right)}{\sqrt{2}\sigma_1}\right]^2-\left[\frac{\hat{e}_2\cdot\left(\vec{x}-\vec{\mu}\right)}{\sqrt{2}\sigma_2}\right]^2\right). \tag{A.2}$$

To express Bingham distribution in a form equivalent to Eq. (A.2), we can rewrite the exponential part of equation of Eq. (10) as

$$\kappa(\mu_1\cdot\hat{n})^2+(\beta-\kappa+\kappa)(\mu_2\cdot\hat{n})^2+(\kappa-\kappa)(\mu_3\cdot\hat{n})^2, \tag{A.3}$$

which simplifies to

$$\kappa-(\kappa-\beta)(\hat{\mu}_2\cdot\hat{n})^2-\kappa(\hat{\mu}_3\cdot\hat{n})^2, \tag{A.4}$$

since $(\hat{\mu}_1\cdot\hat{n})^2+(\hat{\mu}_2\cdot\hat{n})^2+(\hat{\mu}_3\cdot\hat{n})^2=1$. Eq. (A.4) is used to rewrite Eq. (10) as

$$f(\hat{n};\mathbf{B})=\frac{e^\kappa}{c_B}\exp\left(-\frac{(\hat{\mu}_2\cdot\hat{n})^2}{1/(\kappa-\beta)}-\frac{(\hat{\mu}_3\cdot\hat{n})^2}{1/\kappa}\right), \tag{A.5}$$

which has the same form as the probability density function in Eq. (A.2). The dispersion parameters of this equation are $1/(\kappa-\beta)$ and $1/\kappa$, which are proportional to $\sigma_1{}^2$ and $\sigma_2{}^2$ in Eq. (A.2). Since $\kappa\geq(\kappa-\beta)\geq0$, the dispersion extent along $\hat{\mu}_3$ is less than that along $\hat{\mu}_2$.

Appendix B. Eigenvalues of the orientation tensor

An orientation tensor, $\mathbf{T}$ is defined as the second moment (also known as the scatter matrix) of an ODF. In the case of a Bingham distribution,

$$\mathbf{T}=\int_{\mathbb{S}_2}f(\hat{n};\mathbf{B})\hat{n}\hat{n}^{\mathrm{T}}\mathrm{d}\hat{n}\ . \tag{B.1}$$

As $\mathbf{T}$ is symmetric ($(\hat{n}\hat{n}^\top)^\top=\hat{n}\hat{n}^\top$), it can be expressed in a diagonalised form

$$\mathbf{T}=\begin{pmatrix}\hat{\mu}_1 & \hat{\mu}_2 & \hat{\mu}_3\end{pmatrix}\begin{pmatrix}\tau_1 & 0 & 0\\ 0 & \tau_2 & 0\\ 0 & 0 & \tau_3\end{pmatrix}\begin{pmatrix}\hat{\mu}_1{}^\top\\ \hat{\mu}_2{}^\top\\ \hat{\mu}_3{}^\top\end{pmatrix}, \tag{B.2}$$

where the eigenvectors $\hat{\mu}_1,\hat{\mu}_2$ and $\hat{\mu}_3$ are identical to those of matrix $\mathbf{B}$ in the Bingham distribution and τ_1, τ_2 and τ_3 are the eigenvalues. $\tau_1+\tau_2+\tau_3=1$ due to constancy of the trace ($\mathrm{Tr}(\mathbf{T})=1=\mathrm{Tr}(\hat{n}\hat{n}^\top)$).

In the coordinate system the axes of which are the principal eigenvectors of $\mathbf{T}$, the Bingham distribution has a simple form

$$f(\hat{n};\mathbf{B})=\frac{1}{c_B}\exp\left(\kappa(\hat{\mu}_1\cdot\hat{n})^2+\beta(\hat{\mu}_2\cdot\hat{n})^2\right)=\frac{1}{c_B}\exp\left(\kappa\cos^2\theta+\beta\sin^2\theta\cos^2\phi\right), \tag{B.3}$$

while

$$\hat{n}\hat{n}^{\mathrm{T}}=\begin{pmatrix}\cos^2\theta & \sin\theta\cos\theta\sin\phi & \sin\theta\cos\theta\cos\phi\\ \sin\theta\cos\theta\sin\phi & \sin^2\theta\sin^2\phi & \sin^2\theta\sin\phi\cos\phi\\ \sin\theta\cos\theta\cos\phi & \sin^2\theta\sin\phi\cos\phi & \sin^2\theta\cos^2\phi\end{pmatrix}. \tag{B.4}$$

The particular components of $\mathbf{T}$ can be computed by integrating each component of $f(\hat{n};\mathbf{B})\hat{n}\hat{n}^\top$, over the unit sphere. It can be shown that for $i\neq j$, $\mathbf{T}_{ij}=0$, so the diagonal components of $\mathbf{T}$ are equal to the respective eigenvalues, such that

$$\tau_1=\mathbf{T}_{11}=\frac{1}{c_B}\int_0^{2\pi}\mathrm{d}\phi\int_0^1\mathrm{d}\ \cos\theta\ \exp\left(\kappa\cos^2\theta+\beta\sin^2\theta\sin^2\phi\right)\cos^2\theta, \tag{B.5}$$

and

$$\tau_2=\mathbf{T}_{22}=\frac{1}{c_B}\int_0^{2\pi}\mathrm{d}\phi\int_0^1\mathrm{d}\cos\theta\exp\left(\kappa\cos^2\theta+\beta\sin^2\theta\sin^2\phi\right)\sin^2\theta\sin^2\phi, \tag{B.6}$$

while $\tau_3=1-\tau_1-\tau_2$.

Appendix C. Supplementary data

Supplementary data to this article can be found online at http://dx.doi.org/10.1016/j.neuroimage.2016.01.046.

References

Auria, A., Canales-Rodriguez, E., Wiaux, Y., Dirby, T., Alexander, D.C., Thiran, J.-P., Daducci, A., 2015. Accelerated microstructure imaging via convex optimization AMICO in crossing fibers. Proc. 23rd Annual Meeting of the ISMRM. ISMRM, Toronto, Ontario, Canada.

Basser, P.J., Matiello, J., Le Bihan, D., 1994. MR diffusion tensor spectroscopy and imaging. Biophys. J. 66, 259–267.

Billiet, T., Vandenbulcke, M., Mdler, B., Peeters, R., Dhollander, T., Zhang, H., Deprez, S., den Bergh, B.R.V., Sunaert, S., Emsell, L., 2015. Age-related microstructural differences quantified using myelin water imaging and advanced diffusion MRI. Neurobiol. Aging 36 (6), 2107–2121.

Bingham, C., 1974. An antipodally symmetric distribution on the sphere. Ann. Stat. 6, 1201–1225.

Budde, M.D., Annese, J., 2013. Quantification of anisotropy and fiber orientation in human brain histological sections. Front. Integr. Neurosci. 7 (3).

Chang, Y.S., Owen, J.P., Pojman, N.J., Thieu, T., Bukshpun, P., Wakahiro, M.L.J., Berman, J.I., Roberts, T.P.L., Nagarajan, S.S., Sherr, E.H., Mukherjee, P., 2015. White matter changes of neurite density and fiber orientation dispersion during human brain maturation. PLoS ONE 10 (6), e0123656.

Clark, C., Hedehus, M., Moseley, M., 2001. Diffusion time dependence of the apparent diffusion tensor in healthy human brain and white matter disease. Magn. Reson. Med. 24, 1126–1129.

Conel, J.L., 1939. The Postnatal Development of the Human Cerebral Cortex. Harvard University Press, Cambridge, USA.

Cook, P.A., Alexander, D.C., Parker, G.J.M., 2004. Modelling noise-induced fiber-orientation error in diffusion-tensor MRI. Proc. ISBI. IEEE, Arlington, pp. 332–336.

Daducci, A., Canales-Rodríguez, E.J., Zhang, H., Dyrby, T.B., Alexander, D.C., Thiran, J.-P., 2015. Accelerated microstructure imaging via convex optimisation (AMICO) from diffusion MRI data. NeuroImage 105, 32–44.

Eaton-Rosen, Z., Melbourne, A., Orasanu, E., Cardoso, M.J., Modat, M., Bainbridge, A., Kendall, G.S., Robertson, N.J., Marlow, N., Ourselin, S., 2015. Longitudinal measurement of the developing grey matter in preterm subjects using multi-modal MRI. NeuroImage 111 (0), 580–589.

Feinberg, D., Moeller, S., Smith, S., Auerbach, E., Ramanna, S., Gunther, M., Glasser, M., Miller, K., Ugurbil, K., Yacoub, E., 2010. Multiplexed echo planar imaging for sub-second whole brain fMRI and fast diffusion imaging. PLoS One 5, e15710.

Fiala, J., Spacek, J., Harris, K., 2002. Review: dendritic spine pathology: cause or consequence of neurological disorders. Brain Res. Rev. 39, 29–54.

Fisher, N.I., Lewis, T., Embleton, B.J.J., 1987. Bingham distribution. Statistical Analysis of Spherical Data. Cambridge Univ. Press.

Jacobs, B., Driscoll, L., Schall, M., 1997. Life-span dendritic and spine changes in areas 10 and 18 of human cortex: a quantitative golgi study. J. Comp. Neurol. 386, 661–680.

Jacobs, B., Schall, M., Prather, M., Kapler, E., Driscoll, L., Baca, S., Jacobs, J., Ford, K., Wainwright, M., Treml, M., 2001. Regional dendritic and spine variation in human cerebral cortex: a quantitative golgi study. Cereb. Cortex 11, 558–571.

Jelescu, I.O., Veraart, J., Adisetiyo, V., Milla, S.S., Novikov, D.S., Fieremans, E., 2015. One diffusion acquisition and different white matter models: how does microstructure change in human early development based on WMTI and NODDI? NeuroImage 107 (0), 242–256.

Jespersen, S.N., Bjarkam, C.R., Nyengaard, J.R., Chakravarty, M.M., Hansen, B., Vosegaard, T., Østergaard, L., Yablonskiy, D.A., Chr. Nielsen, N., Vestergaard-Poulsen, P., 2010. Neurite density from magnetic resonance diffusion measurements at ultrahigh field: comparison with light microscopy and electron microscopy. NeuroImage 49, 205–216.

Jespersen, S.N., Kroenke, C.D., Østergaard, L., Ackerman, J.J.H., Yablonskiy, D.A., 2007. Modeling dendrite density from magnetic resonance diffusion measurements. NeuroImage 34, 1473–1486.

Jespersen, S., Leigland, L., Cornea, A., Kroenke, C., 2012. Determination of axonal and dendritic orientation distributions within the developing cerebral cortex by diffusion tensor imaging. IEEE Trans. Med. Imaging 31, 16–32.

Kaden, E., Knösche, T.R., Anwander, A., 2007. Parametric spherical deconvolution: inferring anatomical connectivity using diffusion MR imaging. NeuroImage 37, 474–488.

Kleinnijenhuis, M., Zhang, H., Wiedermann, D., Küsters, B., Norris, B.G., van Cappellen van Walsum, A.-M., 2013. Detailed laminar characteristics of the human neocortex revealed by noddi and histology. Proc. 19th Annual Meeting of the OHBM. OHBM, WA, USA, p. 3815.

Koev, P., Edelman, A., 2006. The efficient evaluation of the hypergeometric function of a matrix argument. Math. Comput. 75, 833–846.

Kunz, N., Zhang, H., Vasung, L., R., O.K., Assaf, Y., Lazeyras, F., Alexander, D.C., Hüppi, P.S., 2014. Assessing white matter microstructure of the newborn with multi-shell diffusion MRI and biophysical compartment models. NeuroImage 96, 288–299.

Lazar, M., Lee, J.H., Alexander, A.L., 2005. Axial asymmetry of water diffusion in brain white matter. Magn. Reson. Med. 54, 860–867.

Lemkaddem, A., Daducci, A., Kunz, N., Lazeyras, F., Seeck, M., Thiran, J.-P., Vullimoz, S., 2014. Connectivity and tissue microstructural alterations in right and left temporal lobe epilepsy revealed by diffusion spectrum imaging. NeuroImage 5 (0), 349–358.

Mardia, K., Jupp, P., 1990. Directional statistics. Wiley series in probability and statistics.

Nazeri, A., Chakravarty, M.M., Rotenberg, D.J., Rajji, T.K., Rathi, Y., Michailovich, O.V., Voineskos, A.N., 2015. Functional consequences of neurite orientation dispersion and density in humans across the adult lifespan. J. Neurosci. 35 (4), 1753–1762.

Owen, J.P., Chang, Y.S., Pojman, N.J., Bukshpun, P., Wakahiro, M.L., Marco, E.J., Berman, J.I., Spiro, J.E., Chung, W.K., Buckner, R.L., Roberts, T.P., Nagarajan, S.S., Sherr, E.H., Mukherjee, P., 2014. Aberrant white matter microstructure in children with 16p11.2 deletions. J. Neurosci. 34 (18), 6214–6223.

Pierpaoli, C., Jezzard, P., Basser, P.J., Barnett, A., Di Chiro, G., 1996. Diffusion tensor MR imaging of the human brain. Radiology 201, 637–648.

Riffert, T.W., Schreiber, J., Anwander, A., Knsche, T.R., 2014. Beyond fractional anisotropy: extraction of bundle-specific structural metrics from crossing fiber models. NeuroImage 100 (0), 176–191.

Rowe, M.C., Zhang, H., Oxtoby, N., Alexander, D.C., 2013. Beyond crossing fibers: tractography exploiting sub-voxel fibre dispersion and neighbourhood structure. Information Processing in Medical Imaging. Lect. Notes Comput. Sci. 7917, 402–413.

Schwarz, G., 1978. Estimating the dimension of a model. Ann. Stat. 6, 461–464.

Shoemake, K., 1992. Graphics gems iii. Uniform Random Rotations. Academic Press Professional, Inc., San Diego, CA, USA, Ch, pp. 124–132.

Sotiropoulos, S.N., Behrens, T.E.J., Jbabdi, S., 2012. Ball and rackets: inferring fiber fanning from diffusion-weighted MRI. NeuroImage 60 (2), 1412–1425.

Szafer, A., Zhong, J., Gore, J.C., 1995. Theoretical model for water diffusion in tissues. Magn. Reson. Med. 33, 697–712.

Tariq, M., Kleinnijenhuis, M., van Cappellen van Walsum, A.-M., Zhang, H., 2015. Validation of NODDI estimation of dispersion anisotropy in V1 of the human neocortex. Proc. 23rd Annual Meeting of the ISMRM. Berkeley, USA. ISMRM, Toronto, Canada.

Tariq, M., Schneider, T., Alexander, D.C., Wheeler-Kingshott, C.A.M., Zhang, H., 2014. *In vivo* estimation of dispersion anisotropy of neurites using diffusion MRI. Proceedings of the Annual Meeting of the Medical Image Computing and Computer Assisted Intervention (MICCAI). Boston, USA.

Timmers, I., Zhang, H., Bastiani, M., Jansma, B.M., Roebroeck, A., Rubio-Gozalbo, M.E., 2014. White matter microstructure pathology in classic galactosemia revealed by neurite orientation dispersion and density imaging. J. Inherit. Metab. Dis. 1–10.

Tournier, J.-D., Calamante, F., Connelly, A., 2007. Robust determination of the fibre orientation distribution in diffusion MRI: non-negativity constrained super-resolved spherical deconvolution. NeuroImage 35, 1459–1472.

Türe, U., Yaşargil, M.G., Friedman, A.H., Al-Mefty, O., 2000. Fiber dissection technique: lateral aspect of the brain. Neurosurgery 47 (2), 417–426.

Westin, C.F., Maier, S.E., Mamata, H., Nabavi, A., Jolesz, F.A., Kikinis, R., 2002. Processing and visualization for diffusion tensor MRI. Med. Image Anal. 6 (2), 93–108.

Winston, G.P., Micallef, C., Symms, M.R., Alexander, D.C., Duncan, J.S., Zhang, H., 2014. Advanced diffusion imaging sequences could aid assessing patients with focal cortical dysplasia and epilepsy. Epilepsy Res. 108, 336–339.

Yushkevich, P.A., Piven, J., Hazlett, H.C., Smith, R.G., Ho, S., Gee, J.C., Gerig, G., 2006. User-guided 3D active contour segmentation of anatomical structures: significantly improved efficiency and reliability. NeuroImage 31 (3), 1116–1128.

Zhang, H., Hubbard, P., Parker, G., Alexander, D.C., 2011. Axon diameter mapping in the presence of orientation dispersion with diffusion MRI. NeuroImage 56, 1301–1315.

Zhang, H., Schneider, T., Wheeler-Kingshott, C., Alexander, D., 2012. NODDI: practical *in vivo* neurite orientation dispersion and density imaging of the human brain. NeuroImage 61, 1000–1016.